

**SYNTHESIS, CHARACTERIZATION AND  
INVESTIGATION OF ANTIOXIDANT,  
ANTIBACTERIAL PROPERTIES OF  
DIFFERENT NANOCOMPLEXES LOADED  
WITH 6- THIOGUANINE**

**A Thesis Submitted to the  
Graduate School of İzmir Institute of  
Technology  
in Partial Fulfillment of the Requirements for the Degree of  
MASTER OF SCIENCE  
in Chemistry**

**by  
ZEYNEP SENA ŞİMDİM**

**July 2024  
İZMİR**

We approve the thesis of **Zeynep Sena ŐİMDİM**

**Examining Committee Members:**

---

**Prof. Dr. Őenay ŐANLIER**

Department of Biochemistry, Ege University

---

**Prof. Dr. Ali ŐAĐIR**

Department of Chemistry, İzmir Institute of Technology

---

**Prof. Dr. GölŐah ŐANLI MOHAMED**

Department of Chemistry, İzmir Institute of Technology

**12 July 2024**

---

**Prof. Dr. GölŐah ŐANLI**

**MOHAMED** Supervisor,  
Department of Chemistry İzmir  
Institute of Technology

---

**Prof. Dr. GölŐah ŐANLI MOHAMED**

Head of the Department of Chemistry

---

**Prof. Dr. Mehtap EANES**

Dean of the Graduated School of  
İzmir Institute of Technology

## ACKNOWLEDGMENTS

First of all, I'd like to first I would like to sincerely thank my supervisor, Prof. Dr. Gülşah ŞANLI MOHAMED, for the chance she provided me with as well as for her unwavering patience, support, and encouragement in allowing me to always smile and have confidence in myself. Her advice and all I have learned from her have been priceless. I express my gratitude to the entire personnel and facilities managers of İYTE MAM and BİYOMER for their invaluable assistance and recommendations.

I would like to express my gratitude to the members of the GSM Research Group: Sinem ŞAHİNOĞLU, Ezgi ASLAN, Pınar ÖZTÜRK, Dr. Derya METE and İbrahim Hanif NAZLI.

My special gratitude is extended to my mother Huriye Esra ŞİMDİM, my father Yavuz Ramazan ŞİMDİM and my brother Kerem ŞİMDİM. They gave me the best support possible during my academic career, never withholding their love or encouragement. Without them, it would not have taken place.

## ABSTRACT

### SYNTHESIS, CHARACTERIZATION AND INVESTIGATION OF ANTIOXIDANT, ANTIBACTERIAL PROPERTIES OF DIFFERENT NANOCOMPLEXES LOADED WITH 6-THIOGUANINE

Metal-Organic Frameworks (MOFs) represent a novel class of highly porous molecular structures, 6-TG loaded on these nanoparticles to maximize therapeutic efficacy and reduce toxicity. MOFs are composed of metal ions or clusters connected by multidentate organic bridging ligands, and because of their appealing properties, they have great potential for application in a range of environments, including ZIF-8 and UiO-66. Consequently, the drug-nanocomplex was generated, leading to the formation of 6-TG@ZIF-8 and 6-TG@UiO-66 nanoparticles. These nanoparticles are cationic, biocompatible, biodegradable, immunogenicity-low, and permeability-enhancing.

In addition, bacterial inhibition was investigated using the serial dilution method of 6-TG, 6-TG@ZIF-8 and 6-TG@UiO-66 nanoparticles on the gram-positive bacteria family *Staphylococcus aureus* (*S. aureus*) and the gram-negative bacteria family *Escherichia coli* (*E. coli*) in order to show the effects of antibiotics, dose-response relationships, and the effects of antibacterial resistance. Furthermore, one of the many in vitro test systems used to evaluate antioxidant activity was the DPPH assay, which was used to identify both synthetic and natural compounds having antioxidant properties.

## ÖZET

### **6-Tiyoguanin Yüklü Farklı Nanokomplekslerin Antioksidan, Antibakteriyel Özelliklerinin Sentezi, Karakterizasyonu ve Araştırılması**

Metal-Organik çerçeveler (MOF), çekici nitelikleri nedeniyle ve çok dışli organik köprü ligandlarıyla bağlanan metal iyonları veya kümelerden oluşan oldukça gözenekli moleküler yapılardan oluşan yepyeni bir kategori olarak karşımıza çıkmaktadır ve çeşitli ortamlarda kullanılmak üzere önemli miktarda potansiyele sahip olan ZIF-8 ve UiO-66; anti-neoplastik ve immünoşüpresif aktiviteye sahip sentetik bir guanozin analogu antimetabolit olan 6-TG'nin terapötik etkinliğini arttırmak ve toksisitesini en aza indirmek için 6-TG bu metal organik çerçevelere yüklenmiştir. Böylelikle ilaç-nanokompleksi elde edilerek nispeten toksik olmayan, biyouyumlu, biyolojik olarak parçalanabilen, katyonik, biyo-yapışkan, düşük immünojenite ve geçirgenliği arttırıcı özelliklerine sahip 6-TG@ZIF-8 ve 6-TG@UiO-66 nanopartikülleri oluşturulmuştur.

Buna ek olarak antibiyotiklerin etkisini ve doz-cevap ilişkilerini göstermek ve antibakteriyel direncin oluşturduğu etkileri gözlemlemek için gram negatif bakteri familyasından *Escherichia coli* (*E. coli*) ve gram pozitif bakteri familyasından *Staphylococcus aureus* (*S. aureus*) üzerinde 6-TG,6-TG@ZIF-8 ve 6-TG@UiO-66 nanoparçacıklarının seri dilüsyon yöntemiyle bakteri inhibisyonuna bakılmıştır. Ayrıca, antioksidan etkiye sahip doğal kaynaklı ve sentetik kaynaklı bileşiklerin keşfi için, in vitro olarak yapılan çeşitli test sistemlerinden biri olan DPPH analizi yapılarak antioksidan aktivite test edilmiştir.

# TABLE OF CONTENTS

LIST OF FIGURES .....	ix
LIST OF TABLES .....	viii
LIST OF ABBREVIATIONS .....	vxv
CHAPTER 1. INTRODUCTION .....	1
1.1. Antibacterial Assay .....	1
1.1.1. Agar Dilution.....	2
1.1.2. Broth Dilution and MIC .....	2
1.1.3. Gram-negative and Gram-positive Bacteria .....	3
1.1.3.1. Escherichia coli ( <i>E. coli</i> ) .....	4
1.1.3.2. Staphylococcus aureus ( <i>S. aureus</i> ) .....	4
1.2. Antioxidant Assay .....	5
1.2.1. Methods of Measuring the Antioxidant Capacity .....	6
1.2.1.1. DPPH Assay.....	6
1.2.1.2. ABTS Assay .....	7
1.3. 6-Thioguanine .....	7
1.3.1. Mechanism Action of 6-TG .....	7
1.3.2. Effect of 6-TG on Cancer Cells .....	8
1.4. Metal Organic Frameworks .....	9
1.4.1. Synthesis of MOFs .....	9
1.5. ZIF Family .....	10
1.5.1. ZIF-8 .....	11
1.5.1.1. Antibacterial and Antioxidant Effect of ZIF-8 .....	12
1.6. UiO Family .....	13
1.6.1. UiO-66... ..	14
1.6.2 Antibacterial Effect of UiO-66.....	16
CHAPTER 2. MATERIALS AND METHODS.....	17
2.1. Synthesis and Optimization Synthesized Nanoparticles .....	17

2.1.1. ZIF-8 and 6-TG@ZIF-8 Nanoparticles .....	17
2.1.2. UiO-66 and 6-TG@UiO-66 Nanoparticles .....	17
2.2. Characterization of Synthesized Nanoparticles .....	18
2.2.1. Synthesis Yield of ZIF-8 and UiO-66 Nanoparticles .....	18
2.2.2. Determination of 6-TG Loading Effectiveness .....	18
2.2.3. Structural Analysis .....	19
2.3. Biocompatibility Tests of Synthesized Nanoparticles.....	19
2.3.1. Serum Protein Binding .....	19
2.3.2. Hemolysis Analysis .....	20
2.4. Drug Release of 6-TG@ZIF-8 and 6-TG@UiO-66 Nanoparticles .	20
2.5. Investigation of Antioxidant Activities .....	21
2.6. Investigation of Antibacterial Activities .....	21
2.6.1. Preparation of Nutrient Agar Medium.....	22
2.6.2. Preparation of Tryptic Soy Agar Medium....	22
 CHAPTER 3. RESULT AND DISCUSSION .....	 23
3.1 Synthesis and Optimization Synthesized Nanoparticles .....	23
3.2. Characterization of Synthesized Nanoparticles .....	23
3.2.1. Synthesis Yield of ZIF-8 and UiO-66 Nanoparticles .....	23
3.2.2. Drug Loading Capacity .....	23
3.2.3. Structural Analysis .....	25
3.2.3.1. Scanning Electron Microscopy .....	25
3.2.3.1.1. ZIF-8 and 6-TG@ZIF-8 Nanoparticles .....	25
3.2.3.1.2. UiO-66 and 6-TG@UiO-66 Nanoparticles .....	27
3.2.3.2. Energy Dispersive X-Ray Spectroscopy (EDX).....	28
3.2.3.2.1. ZIF-8 and 6-TG@ZIF-8 Nanoparticles .....	28
3.2.3.2.2. UiO-66 and 6-TG@UiO-66 Nanoparticles .....	29
3.2.3.3. Fourier Transform Infrared Analysis Energy Dispersive X-Ray (FT-IR) .....	29
3.2.3.3.1. ZIF-8 and 6-TG@ZIF-8 Nanoparticles .....	29
3.2.3.3.2. UiO-66 and 6-TG@UiO-66 Nanoparticles .....	30

3.2.3.4. X-Ray Diffraction Device (XRD) .....	32
3.2.3.4.1. ZIF-8 and 6-TG@ZIF-8 Nanoparticles .....	32
3.2.3.4.2. UiO-66 and 6-TG@UiO-66 Nanoparticles.....	33
3.2.3.5. Dynamic Light Scattering Method (DLS) and Zeta Potential.....	34
3.2.3.5.1. ZIF-8 and 6-TG@ZIF-8 Nanoparticles .....	34
3.2.3.5.2. UiO-66 and 6-TG@UiO-66 Nanoparticles.....	35
3.2.3.6. Thermogravimetric Analysis (TGA) .....	35
3.2.3.6.1. ZIF-8 and 6-TG@ZIF-8 Nanoparticles .....	35
3.2.3.6.2. UiO-66 and 6-TG@UiO-66 Nanoparticles .....	36
3.3. Biocompatibility Tests of Synthesized Nanoparticles.....	37
3.3.1. Serum Protein Binding.....	37
3.3.1.1. ZIF-8 and 6-TG@ZIF-8 Nanoparticles .....	38
3.3.1.2. UiO-66 and 6-TG@UiO-66Nanoparticles .....	38
3.3.2. Hemolysis .....	39
3.3.2.1. ZIF-8 and 6-TG@ZIF-8 Nanoparticles .....	39
3.3.2.2. UiO-66 and 6-TG@UiO-66 Nanoparticles .....	40
3.4. Drug Release.....	40
3.4.1. ZIF-8 and 6-TG@ZIF-8 Nanoparticles .....	40
3.4.2. UiO-66 and 6-TG@UiO-66 Nanoparticles .....	41
3.5. Investigation of Antioxidant Activities .....	42
3.5.1. ZIF-8 and 6-TG@ZIF-8 Nanoparticles.....	42
3.5.2. UiO-66 and 6-TG@UiO-66 Nanoparticles .....	43
3.6. Investigation of Antibacterial Activities .....	43
3.6.1. ZIF-8 and 6-TG@ZIF-8 Nanoparticles.....	43
3.6.2. UiO-66 and 6-TG@UiO-66 Nanoparticles.....	45
CHAPTER 4. CONCLUSION.....	47
REFERENCES.....	48

## LIST OF FIGURES

<u>Figure</u>	<u>Page</u>
Figure 1.1. Structure of 6-TG.....	8
Figure 1.2. Structure of Zeolitic Imidazolate Framework.....	12
Figure 3.1. Calibration curve of 6-TG .....	24
Figure 3.2. SEM micrographs of ZIF-8 .....	25
Figure 3.3. SEM micrographs of a) 6-TG@ZIF-8 (1,25 mg/mL) b) 6-TG@ZIF-8 (2,5 mg/mL) c) 6-TG@ZIF-8 (5 mg/mL) d) 6-TG@ZIF-8 (10 g/mL).....	26
Figure 3.4. SEM micrographs of a) ZIF-8 and b) 6-TG@ZIF-8 (5 mg/mL).....	26
Figure 3.5. SEM micrographs of UiO-66 .....	27
Figure 3.6. SEM micrographs of a) 6-TG@UiO-66 (1,25 mg/mL) b) 6-TG@UiO-66 (2,5 mg/mL) c) 6-TG@UiO-66 (5 mg/mL) d) 6-TG@UiO-66 (10 mg/mL).....	27
Figure 3.7. SEM micrographs of a) UiO-66 and b) 6-TG@ UiO-66 (5 mg/mL).....	28
Figure 3.8. FTIR spectra of a) 6-TG, b) ZIF-8 and c) 6-TG@ZIF-8 (5 mg/mL).....	30
Figure 3.9. FTIR spectra of a) 6-TG, b) UiO-66 and c) 6-TG@UiO-66 (5 mg/mL).....	31
Figure 3.10. XRD patterns of a) 6-TG, b) ZIF-8 and c) 6-TG@ZIF-8 (5 mg/mL) .....	32
Figure 3.11. XRD patterns of a) 6-TG, b) UiO-66 and c) 6-TG@UiO-66 (5 mg/mL) .....	33
Figure 3.12. TGA graphs of 6-TG, ZIF-8 and 6-TG@ZIF-8 (5 mg/mL) .....	36
Figure 3.13. TGA graphs of 6-TG, UiO-66 and 6-TG@UiO-66 (5 mg/mL) .....	37
Figure 3.14. Hemolysis rates of 6-TG, ZIF-8 and 6-TG@ZIF-8 (5 mg/mL) .....	39
Figure 3.15. Hemolysis rates of 6-TG, UiO-66 and 6-TG@UiO-66 (5 mg/mL) .....	40
Figure 3.16. Drug release profiles of 6-TG, ZIF-8 and 6-TG@ZIF-8 (5 mg/mL) .....	41
Figure 3.17. Drug release profiles of 6-TG, UiO-66 and 6-TG@UiO-66 (5 mg/mL) .....	41
Figure 3.18. Antioxidant activities of 6-TG, ZIF-8 and 6-TG@ZIF-8 (5 mg/mL) .....	42
Figure 3.19. Antioxidant activities of 6-TG, UiO-66 and 6-TG@UiO-66 (5 /mL) .....	43
Figure 3.20. Antibacterial activities of 6-TG, ZIF-8 and 6-TG@ZIF-8 on S. aureus... ..	44
Figure 3.21. Antibacterial activities of 6-TG, ZIF-8 and 6-TG@ZIF-8 on E. coli .....	44
Figure 3.22. Antibacterial activities of 6-TG, UiO-66 and 6-TG@UiO-66 on S. aureus.....	46

Figure 3.23. Antibacterial activities of 6-TG, UiO-66 and 6-TG@UiO-66 on E. coli..... 46

## LIST OF TABLES

<b><u>Table</u></b>	<b><u>Page</u></b>
Table 3.1. 6-TG Loading Capacity of 6-TG@ZIF-8 Nanoparticles.....	24
Table 3.2. 6-TG Loading Capacity of 6-TG@UiO-66 Nanoparticles.....	24
Table 3.3. EDX curves and elemental compositions of ZIF-8 and 6-TG@ZIF-8 (5 mg/mL).....	28
Table 3.4. EDX curves and elemental compositions of ZIF-8 and 6-TG@ZIF-8 (5 mg/mL).....	29
Table 3.5. Hydrodynamic radius and zeta potentials of ZIF-8 and 6-TG@ZIF-8 (5 mg/mL).....	34
Table 3.6. Hydrodynamic radius and zeta potentials of UiO-66 and 6-TG@UiO-66 (5 mg/mL).....	35
Table 3.7. Protein Binding (%) of 6-TG, ZIF-8 and 6-TG@ZIF-8 (5 mg/mL) .....	38
Table 3.8. Protein Binding (%) of 6-TG, UiO-66 and 6-TG@UiO-66 (5 mg/mL) .....	39

## LIST OF ABBREVIATIONS

MIC	Minimal Inhibitory Concentration
E. coli	Escherichia coli
S. aureus	Staphylococcus aureus
ROS	Reactive Oxygen Species
DPPH	2,2-Diphenyl-1-picrylhydrazyl
ABTS	2,2'-Azino-bis (3-ethylbenzothiazoline-6-sulfonic acid)
6-TG	6-thioguanine (6-TG) or thioguanine
MOF	Metal–Organic Framework
SBU <sub>s</sub>	Secondary Building Units
DMF	Dimethylformamide
PS	Zinc Phthalocyanine
NPs	Nanoparticles
EtOH	Ethanol
DMSO	Dimethyl Sulfoxide
DLS	Dynamic Light Scattering
SEM	Scanning Electron Microscopy
EDX	Energy Dispersive X-Ray Spectroscopy
XRD	X-ray Diffraction
TGA	Thermogravimetric Analysis
FTIR	Fourier-Transform Infrared Spectroscopy
EDTA	Ethylenediaminetetraacetic acid
PBS	Phosphate Buffered Saline
FBS	Fetal Bovine Serum
TSA	Tryptic Soy Agar
NA	Nutrient Agar

# CHAPTER 1

## INTRODUCTION

The aim of this study is that metal-organic frameworks (MOFs) represent a novel class of highly porous molecular structures, 6-TG loaded on these nanoparticles to maximize therapeutic efficacy and reduce toxicity. MOFs are composed of metal ions or clusters connected by multidentate organic bridging ligands, and because of their appealing properties, they have great potential for application in a range of environments, including ZIF-8 and UiO-66.

Furthermore, in order to demonstrate the effects of antibiotics, dose-response relationships, and antibacterial resistance, bacterial inhibition was examined using the serial dilution method of 6-TG, 6-TG@ZIF-8, and 6-TG@UiO-66 nanoparticles on the gram-positive bacteria family *Staphylococcus aureus* (*S. aureus*) and the gram-negative bacteria family *Escherichia coli* (*E. coli*). Furthermore, the DPPH assay, which was used to find both synthetic and natural substances having antioxidant capabilities, was one of the several in vitro test systems used to investigate antioxidant activity.

### 1.1. Antibacterial Assay

Antibiotics have transformed human health by making it possible to treat infections that may be fatal. Finding novel antibiotics is now necessary, though, as bacterial resistance to existing medicines is becoming more common. The majority of antibiotics on the market today have natural origins, particularly from different marine or microbial sources. Additionally, plants create defense mechanisms against microbes. A straightforward, quick, accurate, dependable, sensitive, safe, and economical in vitro antibacterial test must be used to screen natural products, such as crude extracts, chromatographic fractions, or purified chemicals, for antibacterial activity (Drummond A.J. & Waigh R.D., 2000).

### **1.1.1. Agar Dilution**

The two most widely used methods for figuring out the minimal inhibitory concentration (MIC) of antimicrobial agents—which include antibiotics and other drugs with bactericidal or bacteriostatic properties—are agar and broth dilution. Unlike other antimicrobial biocides like preservatives and disinfectants, the techniques outlined here are intended to determine sensitivity to antibiotic agents. They can, nevertheless, be utilized with these other antimicrobials for no significant reason. Agar dilution involves directly spotting solutions containing predetermined quantities of bacterial cells onto nutritional agar plates with varying concentrations of antibiotics. Bacterial colonies on the plates after incubation are a sign of the organism's growth (Wiegand, 2007).

### **1.1.2. Broth Dilution and MIC**

In the broth dilution method, a specific number of bacterial cells are included into a liquid growth medium that contains geometrically increasing concentrations of the antimicrobial drug. This is usually achieved through a series of twofold dilutions. When employing a total volume of 2 ml, the test's final volume determines whether the procedure is referred to as macro dilution or micro dilution when it is carried out in microliter plates with < 500 ml per well. The organism is growing after incubation if there is turbidity or sediment present. The minimum inhibitory concentration (MIC), as determined by the antimicrobial agent's concentration in milligrams per liter (mg/ml) under specific conditions, is the same for both the broth dilution and agar dilution methods. Antibiotic medication resistance can be tracked using minimum inhibitory concentration (MIC) measurements (Wiegand, 2007). According to Wiegand et al. (2008), dilution methods are used to assess the efficacy of different susceptibility testing techniques as well as serving as reference methods for in vitro susceptibility testing.

Based on clinical and microbiological experience, breakpoints—the specific MIC that separates susceptible and presumed to be treatable organisms from resistant and presumed to be untreatable organisms—can change depending on the specific species under investigation and the antimicrobial agent in use.

The MIC distributions of pertinent species, the antimicrobial agent's pharmacodynamics and pharmacokinetics, and clinical outcome data are characteristics

that determine these breakpoints. Susceptibility is linked to a higher chance of treatment success, while resistance (beyond the breakpoint) is linked to a higher risk of therapeutic failure (Kahlmeter, 2003).

MIC values can be employed to monitor the emergence of antibiotic medication resistance. The calculation of minimum inhibitory concentration (MIC) is a useful tool for resistance surveillance since even little changes can have a clinically significant impact. It also serves as a useful comparison for different forms of a particular antimicrobial agent and/or species that exhibit varying degrees of susceptibility. The MIC determination is, in fact, one of the initial steps in assessing the antibacterial potential of novel drug candidates (Kahlmeter, 2003).

### **1.1.3. Gram-negative and Gram-positive Bacteria**

Bacteria are prokaryotic single-celled organisms without a distinct nucleus or many organelles. Bacterial cell walls and plasma membranes make up their cell envelope. The cell wall's main job is to shield the bacteria from internal pressure. Bacteria are categorized as either Gram positive or negative type based on their structure and properties of their cell walls. In contrast to Gram-negative bacteria, which have peptidoglycan cell walls that are less than 10 nm, Gram-positive bacteria have thicker but porous cell walls (20–80 nm) (Breijyeh Z. et al., 2020; Prochnow-Mai A. et al., 2016). Large molecules cannot pass through the extra outer membrane that Gram-negative bacteria have, in contrast to Gram-positive bacteria (Pajerski W. et al., 2019). A popular method for separating the two kinds of bacteria according to the properties of their cell walls is gram staining. The main stain employed in this method, crystal violet, has big molecules that are unable to pass through the thick peptidoglycan coating of Gram-positive bacteria, leaving the bacteria's cells purple-stained. On the other hand, Gram-negative bacteria's thin peptidoglycan coating prevents them from holding onto the main dye. Gram-positive cells maintain their purple color after decolorization and recoloring with safranin, but Gram-negative cells take on a pink hue (Thairu Y. et al., 2014). Gram-negative bacteria are more harmful due to their cell wall characteristics, which also make them less vulnerable to antibiotics (Lambert P.A., 2002).

### **1.1.3.1. Escherichia Coli (E. coli)**

The microbe that has been studied the most is *Escherichia coli*. It is one of the most significant infections in humans as well as a frequent commensal habitant of the gastrointestinal tract. Thus, among Gram-negative bacteria (GNB), *E. coli* is the most common cause of urinary tract infections (UTIs) and bloodstream infections. These isolates have unique virulence characteristics that commensal and intestine pathogenic strains lack, such as adhesins, toxins, iron-acquisition systems, polysaccharide coatings, and invasions (Sannes et al. 2004).

Furthermore, according to Guiral et al. (2011), *E. coli* is the enteric Gram-negative bacilli that are most commonly discovered in the genital tracts of women. These bacteria can cause vaginal and/or endocervical colonization, as well as various infections in pregnant women, including intra-amniotic and puerperal infections, and infections in infants, including early and late neonatal sepsis.

The antimicrobial drugs that have been used in human and veterinary treatment for the longest, such as ampicillin, have consistently been associated with the highest levels of antibiotic resistance in *E. coli*. But over the last 20 years, there have been increases in the appearance and dissemination of bacteria that are resistant to multiple drugs. These bacteria include strains that are resistant to more recent antibiotics such as fluoroquinolones and extended-spectrum cephalosporins (Levy and Marshall 2004).

### **1.1.3.2. Staphylococcus Aureus (S. aureus)**

Gram-positive, cocci-shaped bacteria that are stained purple by Gram stain are known as *Staphylococcus aureus*. These bacteria are typically seen in clusters that are referred to as "grape-like." These organisms may thrive on media in up to 10% salinity; colonies are commonly yellow or golden in color (the word "aureus" refers to these colors). These organisms may survive at temperatures ranging from 18 to 40 degrees Celsius, both aerobically and anaerobically (facultatively) (Lowy FD, 1998; Rasigade JP & Vandenesch F, 2014).

As one of the most prevalent bacteria in the world, *S. aureus* is the source of many human infections, such as bacteremia, infective endocarditis, infections of the skin and soft tissues (such as impetigo, folliculitis, furuncles, carbuncles, cellulitis, scalded skin

syndrome, and others), osteomyelitis, septic arthritis, infections from prosthetic devices, infections of the lungs (such as pneumonia and empyema), gastroenteritis, meningitis, toxic shock syndrome, and urinary tract infections (Tong SY et al., 2015).

## **1.2. Antioxidant Assay**

Reactive oxygen species (ROS) generation and buildup within cells is referred to as oxidative stress. According to Hill et al. (2018), ROS, such as superoxide ( $O_2^-$ ), hydrogen peroxide ( $H_2O_2$ ), and hydroxyl radical (OH), cause lipid peroxidation, DNA hydroxylation, protein denaturation, and eventually apoptosis, all of which impact cell viability. According to Liguori et al. (2018), oxidative damage to biological macromolecules causes aging and is linked to a number of illnesses, including as cancer, atherosclerosis, cardiovascular conditions, and inflammatory diseases. Exogenous antioxidants from the food can eliminate the consequences of ROS-free radical reactions even if they can be stopped by a variety of endogenous mechanisms (Kurutas, 2016). Lactic acid bacteria (LAB) strains are prominent probiotics that slow down aging by responding quickly and sensitively to oxidative stress. According to Ding et al. (2017), it has anti-inflammatory and antioxidative properties.

In the host intestine, they demonstrate strong antioxidant activity and stimulate the synthesis of antioxidant compounds that aid in the elimination of reactive oxygen species (ROS), thereby mitigating oxidative damage and minimizing disorders linked to oxidative stress (Feng and Wang, 2020; Wang et al., 2017).

Antioxidant characteristics can be measured using biochemical techniques based on several mechanisms. Antioxidant properties are expressed as antioxidant capacity, antioxidant power, and antioxidant potential. (i) Spectroscopic techniques (such as 2,2-diphenyl-1-picrylhydrazyl (DPPH), 2,2-azinobis, 3-ethyl-benzothiazoline-6-sulfonic acid) (ABTS), ferric reducing antioxidant power (FRAP), potassium ferricyanide reducing antioxidant power (PFRAP), and copper reducing antioxidant power (CUPAC) analyzes; (ii) Electrochemical techniques (cyclic; voltammetry, amperometry, bio-amperometry and biosensor methods) (Chistyakov et al., 2018); (iii) Chromatography techniques (GAS Chromatography, HPLC, and total oxidant scavenging capacity (TOSC) method); (iv) Fluorescence Methods (total radical scavenging); antioxidant parameter (TRAP) assay, oxygen radical absorbance capacity

(ORAC) assay, and hydroxyl radical inhibition capacity (HORAC) (Apetrei and Munteanu, 2021) ; v) Additional analytical techniques, like crocin bleaching (Prieto et al., 2015), acidic potassium permanganate (Adcock et al., 2014), autographic (Zampini et al., 2010), permanganate-reducing antioxidant capacity (PRAC) (Cacig et al., 2006; Kasote et al., 2019; Popović et al., 2012), and potassium permanganate agar (Zhou et al., 2015) are some of the other analytical techniques that have been developed for complex samples.

### **1.2.1. Methods of Measuring the Antioxidant Capacity**

Many methods are used to determine the antioxidant activity of substances, but among these methods, two are preferred because they provide results in a shorter time; These are DPPH assay and ABTS assay.

#### **1.2.1.1. DPPH Assay**

The DPPH assay is a well-known and traditional technique for determining antioxidant capacity. It was first applied in the 1950s to find H-donors in natural sources and may be easily modified for polyphenol research (Pyrzynska A. & Pekal A., 2013). This assay's mechanism is that the presence of antioxidants that donate hydrogen would cause DPPH• to change into non-radical DPPH-H, which would cause the color to change from purple to yellow and decrease UV absorption. As a result, the assessment of the absorbance value at 517 nm can provide insight into the antioxidant capacity. The findings are typically expressed as EC<sub>50</sub>, or the quantity of tested antioxidant that could reduce the initial DPPH• concentration by 50%, or standardized by the Trolox equivalent unit (TE) (Schaich K.M. et al., 2015). Small molecular polyphenols with lipophilic properties, such as quercetins, resveratrols, and anthocyanins, can have their antioxidant capacity measured using the DPPH assay; however, this method is limited for those with little or no lipophilic characteristic. As a result, a water-ethanol mixed solvent was studied for the DPPH test (Stasko A. et al., 2007).

However, as DPPH• would coagulate with a specific amount of water, the water to ethanol ratio needs to be precisely controlled.

### **1.2.1.2. ABTS Assay**

Miller et al. employed ABTS for the first time to measure a substance's overall antioxidant capacity in vitro (Miller N.J. et al., 1993). The chromogenic agent in this procedure is ABTS. The persistent blue-green cationic radical  $ABTS^+$  is produced following the oxidative reaction with potassium persulfate and exhibits significant absorption at 734 nm. Since antioxidants decolorize  $ABTS^+$  through radical scavenging, the absorbance value at 734 nm decreases, which indicates the antioxidant capacity (Ilyasov I.R. et al., 2020; Ivekovic D. et al., 2005). Lastly, the outcomes are contrasted with the Trolox control standard system, which uses a water-soluble chemical that is comparable to VE. The results are primarily reported as the Trolox equivalent antioxidant capacity (TEAC) (Schaich K.M. et al., 2015). The ABTS method is widely used to determine the antioxidant capacity of polyphenols because it works well with both lipophilic and hydrophilic antioxidants, requires little in the way of instruments and equipment, and has a strong correlation with the biological activity of antioxidants (Tian X. & Schaich K.M., 2013). To fully assess the antioxidant capability, this method should be used in conjunction with other techniques.

## **1.3. 6-Thioguanine**

6-Thioguanine (6-TG) is an artificial guanosine analogue antimetabolite that has immunosuppressive and anti-neoplastic properties. It is frequently used to maintain treatment for lymphoblastic non-Hodgkin lymphoma and pediatric acute lymphoblastic leukemia (ALL) (Karran P., 2008; Munshi P.N., 2014). 6-TG is useful against mutant tumors of breast cancer types 1 or 2 (BRCA1 or BRCA2) that are resistant to platinum-based chemotherapy or poly (ADP-ribose) polymerase (PARP) inhibitors (Issaeva N. et al., 2010), inhibits ubiquitin-specific protease 2 (USP2), which accumulates in cancer and a key therapeutic target.

### **1.3.1. Mechanism Action of 6-TG**

Hypoxanthine-guanine phosphoribosyltransferase (HGPRTase) is the enzyme

that 6-thioguanine uses to convert to 6-thioguanosine monophosphate (TGMP). Elevated levels of TGMP have the potential to build up inside cells and interfere with the enzyme Inosine monophosphate dehydrogenase (IMP dehydrogenase)'s ability to synthesize guanine nucleotides, which can result in mutations in DNA (Evans WE, 2004).

Thioguanosine diphosphate (TGDP) and thioguanosine triphosphate (TGTP) are produced through the phosphorylation of TGMP. Deoxyribosyl analogs are simultaneously produced by the ribonucleotide reductase enzyme. 6-thioguanine nucleotides (6-TGN) is the collective term for the TGMP, TGDP, and TGTP. 6-TGN block the GTP-binding protein (G protein), Rac1, which controls the Rac /Vav pathway, and are lethal to cells via (1) incorporation into DNA during the synthesis phase (S-phase) of the cell (de Boer NK et al., 2007).

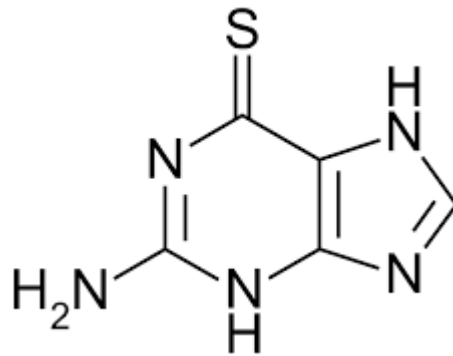


Figure 1.1. Structure of 6-TG

### 1.3.2. Effect of 6-TG on Cancer Cells

According to recent research, 6-TG specifically destroys tumors that are BRCA1 and BRCA2 deficient, including ovarian and breast malignancies (Issaeva N. et al., 2010; Yamane K. et al., 2007). 6-TG is transformed into 6-thioguanine nucleotide (6-TGN), which is then integrated into mammalian cells' nucleic acid (Warren D.J. et al., 1995). Following its in situ methylation to 6-meTG, the integrated 6-TG serves as a substrate for mismatch repair (MMR). 6-TG damages DNA in cancer cells and induces single and double strand breaks (DSBs). NF-κB is activated in response to DNA damage, and one of its primary purposes in this context is to prevent injured cells from going into suicide. On the other hand, anticancer medication resistance, cell invasion, proliferation, and anti-apoptotic mechanisms are linked to

NF- $\kappa$ B activation in cancer cells. Therefore, in order to maximize its efficacy and reduce its toxicity, an alternate form of 6-TG is needed. Research into loading nanoparticles into medications is one possibility.

## **1.4. Metal Organic Frameworks**

In view of these appealing characteristics, Metal-Organic Frameworks (MOFs) represent a novel class of highly porous molecular structures made of metal ions or clusters connected by multidentate organic bridging ligands, with considerable potential applications in diverse contexts. MOFs have been suggested as a viable solution to lessen the drawbacks of alternative drug delivery systems because of their potential to demonstrate low toxicity, good clearance, high drug loadings, and ease of functionalization (Lazaro Ab<sup>n</sup> anades I. et al., 2020). They are also widely employed in many other industries, including the storage of hydrogen, because of the special qualities of different compositions, their suitability for surface modification, their maximum load capacity and surface area, their tunable porosity, their biocompatibility, and their biodegradability. Also, they have two structural aspects; one of them is the primary building units and the other one is secondary building units.

### **1.4.1. Synthesis of MOFs**

As previously mentioned, MOFs are made up of two main parts: organic linkers, also known as bridging ligands, and metal ions. Traditionally, to create a crystalline and porous network, metal ions and organic linkers are combined in mild circumstances to create MOFs. The phrase "Modular Synthesis" refers to this (Sumida K et al., 2012). To create these materials, several synthesis techniques have been developed and used during the past 20 years. These can be broadly divided into two categories: traditional, solvothermal methods and non-conventional methods. In addition to these approaches, other routes have also been tried. Differential pathways may result in morphologies, adsorption characteristics, and variations in particle size, size distribution, and crystallization rate, all of which may impact the material's attributes. For instance, the ability of molecules to separate, adsorb, and exhibit catalytic activity can all be directly impacted by the diffusion of guest molecules in porous materials with varying particle

sizes.

## 1.5. ZIF Family

In recent times, nanomaterials have gained significant attention in the biomedical area due to their unparalleled benefits. They are considered a potent tool for diagnosing and treating a wide range of illnesses (Lee D.E. et al., 2012). For instance, a great deal of research has been done on the biomedical uses of porous materials like metal-organic frameworks (MOFs) in an effort to create novel drug formulations that function better biologically than conventional medications (Cai W. et al., 2019a; Lu K. et al., 2018; Zhou J. et al., 2018).

Zeolitic imidazolate frameworks (ZIFs) represent a subclass of metal-organic frameworks (MOFs) that exhibit favorable characteristics like elevated porosity, superior mechanical and thermal stability, adjustable surface properties, and remarkable chemical stability due to their strong resistance against organic solvents and alkaline water (Park K.S. et al., 2006). These characteristics make ZIFs good candidates for numerous applications, including catalysis (Chizallet C. et al., 2010) and gas capture (Banerjee R. et al., 2009), separations (Li Y. et al., 2010), chemical sensors (Lu G. & Hupp J.T., 2010), and medication delivery.

ZIFs originate from the coordination of imidazole (Im) anions and  $M^{2+}$  cations. Im,  $M(\text{Im})_4$  functions as a linker to create connecting bridges between the metal centers of tetrahedral units. This is explained structurally (Kaneti Y.V. et al., 2017; Park K.S. et al., 2006). ZIFs are mostly made of organic materials (Cravillon J. et al., 2009; Park K.S. et al., 2006) and are made in aqueous solutions using solvothermal techniques (Pan Y. et al., 2011).

ZIF functioning has been widely controlled by linker changes or encapsulation of guest species (e.g., nanoparticles (NPs) within ZIFs). Furthermore, ZIFs' pore sizes are readily adjustable, enabling massive cargo loading and tunable mass transfer and molecular diffusion (Karagiari O. et al., 2012; Yang J. et al., 2017). The application of ZIFs in medication delivery and catalysis research has significantly increased due to this special property (Cai W. et al., 2019b; Yao J. et al., 2015).

For the creation of pH-sensitive drug delivery systems (DDSs), ZIFs' stability under

physiological settings and pH-dependent degradability under acidic conditions make them a particularly appealing option (Cai W. et al., 2019b; Zhuang J. et al., 2014). Furthermore, the recent remarkable developments on ZIF-derived nanocomposites are explored, addressing the important issues and viewpoints surrounding these materials. Special attention is paid to the multifunctionality of nanocomposites in the diagnosis and treatment of diseases that are difficult to treat, as well as the potential applications of ZIFs in biomedicine and future steps towards the development of novel nanomedicines. We assume that additional study will help the scientific community become more knowledgeable.

### 1.5.1. ZIF-8

A typical ZIFs material is ZIF-8, which was first synthesized and given the name MAF-4 by the Chen group (Huang X.C. et al., 2006). Later, after doing a thorough investigation, the Yaghi research group formally designated it ZIF-8 (Park K.S. et al., 2020). ZIF-8 has the chemical formula  $Zn(MeIm)_2$ , which is made up of the metal atom Zn and 2-methylimidazole (Phan A. et al., 2010; Venna S.R. et al., 2010). ZIF-8 has simpler and richer synthesis methodologies than other MOF materials. ZIF-8 also benefits substantially from its structure made up of strong linkages, which gives it greater chemical and hydrothermal resilience. As an illustration of its thermal resilience, ZIF-8 can withstand temperatures as high as 500°C without losing structural integrity. Furthermore, ZIF-8 maintains its porosity and crystallinity even after being dissolved in a variety of solutions, including organic solvents and water (Banerjee R. et al., 2008, 2009; Troyano J. et al., 2019).

ZIF-8 can be readily modified because of its easily tunable pore sizes and shapes. Furthermore, the application range of conventional microporous ZIF-8 is significantly increased by the invention of mesoporous and multistage porous ZIF-8. On the surface of ZIF-8, there are several active spots and facial charge separation. ZIF-8 materials are now widely employed in many vital fields and come in various forms, such as powders, colloid, membranes, or thin films (Schelling M. et al., 2020). ZIF-8's distinct physical structure and chemical characteristics offer a suitable platform for its design and investigation in photocatalytic and adsorption systems. ZIF-8 also performs well in various areas like catalysis, treatment, separation, and storage

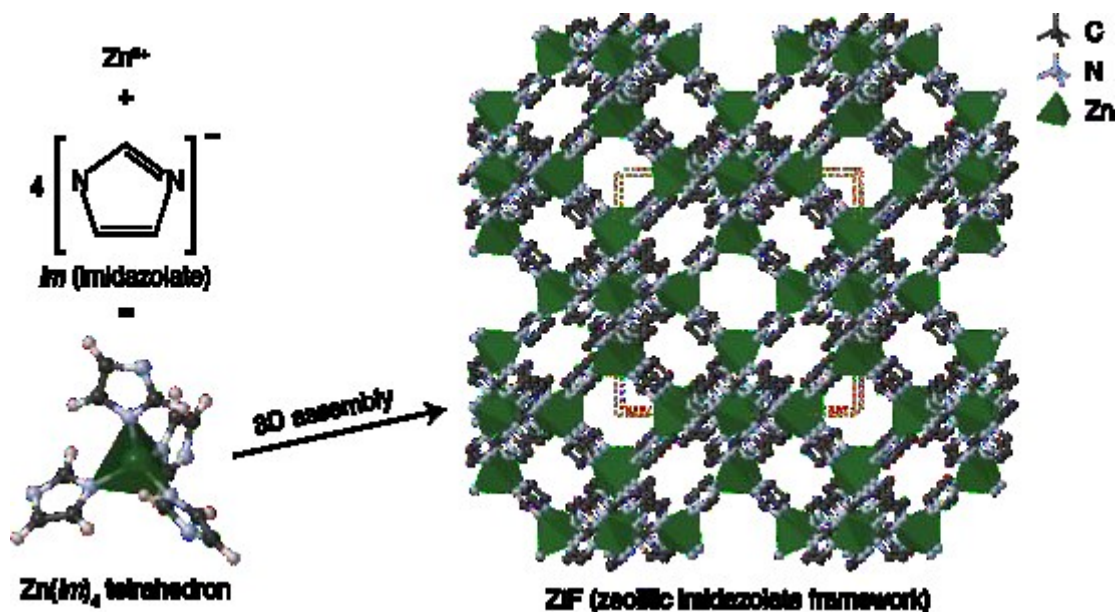


Figure 1.2. Structure of Zeolitic Imidazolate Framework

### 1.5.1.1. Antibacterial and Antioxidant Effect of ZIF-8

It's interesting to note that ZnO nanoparticles and Zn-based MOF have similar antibacterial mechanisms. The production and release of ROS through photocatalysis and the build-up of Zn-based MOFs or ZnO nanoparticles on the cell membrane, which physically harms bacterial cells and enhances the antibacterial impact, are examples of the bactericidal effects (Mendes C.R. et al., 2022; Riduan S.N. & Zhang Y., 2021). Zn-based MOFs were extensively employed in antibacterial chemical delivery systems. Nevertheless, Zn-based MOFs might potentially undergo additional modifications to improve their antibacterial activity. According to the results of the antibacterial activity test, ZIF-8 demonstrated outstanding antibacterial activity against *S. aureus* and *E. coli* (Yao S. et al., 2021). Zn-MOF-based antibacterial fiber exhibits significant promise for use in antimicrobial textile applications. Zheng et al. used the spinning approach with the ZIF-8 and SA mixture to create the very effective antibacterial ZIF-8@alginate fiber (ZIF-8@SA). When tested against *E. coli*, the ZIF-8@SA fiber exhibited outstanding antibacterial activity. MOFs have several advantages for antimicrobial applications, but their high specific surface area, high porosity, tunable size, and designability are the primary ones that determine their benefits. In addition, these characteristics provide them an advantage over other antibacterial materials in terms of durability, targeting, responsive drug release, and multifunctional surfaces (Zheng X. et al., 2020).

The oxidative balance of cells can be upset by overexpressed ROS (such as  $\text{H}_2\text{O}_2$ ,  $\bullet\text{OH}$ , and  $\text{O}_2\bullet^-$ ), which can result in pathogenic diseases. To reduce excessive ROS and mitigate oxidative stress, MOF-based nano enzymes with antioxidant enzyme-like activities, such as GPx, SOD, and CAT-like activities, present a potential option. Neutralizing ROS can reduce inflammation, which is typified by increased generation of reactive oxygen species, and impede the advancement of the disease.

Furthermore, oxidative damage to brain tissues can result in the loss or destruction of neurons, which is the root cause of a number of neurological illnesses. MOF-based nano enzymes have shown promise as neuroprotective nano-agents. Many neurological conditions, such as Alzheimer's disease (Yu et al., 2020), Parkinson's disease (Jiang et al., 2023), ischemic stroke (Wang et al., 2023), central post-stroke pain (Bai et al., 2024), and others, have been treated using these nano enzymes. For example, Zhang's group pyrolyzed metal-doped ZIF-8 to create single atom nano enzymes containing M-N<sub>4</sub> active centers, such as RhN<sub>4</sub>, VN<sub>4</sub>, and Fe-Cu-N<sub>6</sub>.

By inducing vascular endothelial growth factor, regulating immune cell responses, and reducing inflammation, these nano enzymes were incorporated into polyglycolic acid sutures and administered to the scalps of living mice suffering from traumatic brain injury, hastening the healing of scalp wounds (Zhang et al., 2022a). To treat spinal cord injury, Liao's group employed a zinc-organic framework-based aggregation induced emission nano enzyme. This resulted in a sustained release of gallic acid and Zn<sup>2+</sup> at the injury site, promoting antioxidant, reducing inflammation, and assisting in neuronal regeneration (Zheng et al., 2024).

## 1.6. UiO Family

Coordination polymers of the zirconium-carboxylate-based MOF family are called UiO (University of Oslo). Among the popular zirconium-based MOFs employed for the adsorptive removal of environmental contaminants are UiO-66, UiO-67, and UiO-68 (Duo et al., 2018; Mao et al., 2019; Mehta et al., 2019). According to Elrasheedy et al. (2019), they have remarkable thermal stability in addition to significant chemical stability. They also have good mechanical stability and are very porous. Zr<sub>6</sub>O<sub>4</sub>(OH)<sub>4</sub> cluster is used as the metal center and 2-aminoterephthalic acid is used as the ligand to create UiO-66-NH<sub>2</sub>, a metal-organic skeleton material that has great chemical and

thermal stability (Burtch et.al.,2014). UiO-66-NH<sub>2</sub> is primarily meso- and microporous, and the majority of PPCPs have tiny molecules. As a result, UiO-66-NH<sub>2</sub> is frequently employed to extract medicines from water.

### 1.6.1. UiO-66

Zirconium oxide knots joined by terephthalic acid (1,4-benzene dicarboxylic acid (BDC) bridges form the basic crystal known as UiO-66 (Winarta J. et al., 2020). The hydroxylated form of UiO-66 is the most stable of the several forms. UiO-66 crystals have a face-centered cubic lattice with dimensions of 20.7 Å and a symmetry of  $fm\bar{3}m$ . With pore openings of 7.5 and 12 Å and 6 Å, respectively, two frame lattices can be defined: tetrahedron and octahedron (Valenzano L. et al., 2011). Theoretically, the pore volume and surface area are 0.77 cm<sup>3</sup> / g and 1160 m<sup>2</sup>/g, respectively; however, these values differ during works based on preparation conditions (Wu H. et al., 2013).

According to UiO-66's reticular chemistry structure source (RCSR) categorization, the inorganic node is a secondary structure unit in its face centered unit topology. The cuboctahedron structure of the zirconium oxide node gave the BDC 12 ports and allowed for amazing coordination. Eight oxygens make up hydroxylated UiO-66; four are bound to three zirconium atoms independently, while the remaining four are bonded as hydroxides (Furukawa H. et al., 2013). Heat can be used to speed up the process that causes two oxygen atoms to exit the unit along with the hydrogen atoms, leaving the remaining six atoms bound to the zirconium atoms, converting the hydroxylated state to the dehydroxylated state.

Furthermore, it has been shown that a phase transition may place upon a change in shape, meaning that dehydration may couple, but not concurrently (Prats-Platero A.E. et al., 2016).

Diffusion, solvothermal, and modified techniques were the three steps of UiO-66 preparation development (Choi S. et al., 2016). According to Deshpande M.S. et al. (2008), the first technique is also known as the homogeneous phase, in which diffusion of solvents happens as a result of gradual evaporation. Large-sized, supersaturated single crystals are the end outcome. High control over the size, crystallinity, and shape of the particles is provided by the second method, which is now commonly employed and is referred to as hydrothermal (Liang W. et al., 2013). According to Klinowski J. et al.

(2011), the latter comprise a variety of methods including supersonic, mechanical milling, microwave coupled, and electrochemical. Furthermore, by including novel composites, MOFs can work in concert with other materials to support or improve their existing qualities.

Accordingly, the synthesis methods for plain and functionalized UiO-66 varied based on the technique used, solvent, environmental factors, added compounds, and co-modulators (Zou D. & Liu D., 2019).

Zirconium tetrachloride was mixed with terephthalic acid in N, N-dimethylformamide (DMF) solvent in low concentrations of metal and binder, without the addition of any modification ingredients, in the original production of UiO-66. There are no specific preparatory requirements mentioned here. Nonetheless, there has been a greater focus on finding ways to adjust the structure and enhance synthesis (Kandiah M. et al., 2010). Reactants react quickly when added in high quantities, resulting in the formation of an amorphous (gel-like) MOF.

According to Garibay S.J. & Cohen S.M. (2010), this structural form's quick nucleation and connectivity prevent long-distance sorting because to linker dissociation and inadequate repair.

Since UiO-66 is known to be a very stable material, defect engineering has been developed to overcome its inertness (Bueken B. et al., 2017). Here, imperfections make UiO-66 less stable and crystallinity but more useful, adaptable to different substrates, and hydrophilic. According to Shearer G.C. et al. (2016), there are two varieties of defect engineering: incomplete linker and incomplete cluster. As previously noted, UiO-66 contains 12 linkers, which theoretically provides a very stable structure. If any ligands were absent, the structure remained unaffected and the crystal's framework could still be supported by the ligands that were there. Lewis acid sites rise and water and heat resistance fall as the number of flaws rises (Thornton A.W. et al., 2016).

On the contrary, pore size and surface area increase in tandem with a rise in node defects (Øien S. et al., 2014). Simulation studies show that compared to incomplete linkers, the incomplete cluster defect produces a larger surface area product. The counter ion is mostly to blame for the charge balance problem, a recent development (Liu L. et al., 2019). Research has shown conflicting views regarding the source of this ion, which may originate from water, modulators, ambient solvent, and zirconium salt chlorine (Cliffe M.J. et al., 2014).

## 1.6.2. Antibacterial Effect of UiO-66

Utilization of antibiotics can result in illnesses from germs that are resistant to many drugs. Huihui Lv et al. created an antibacterial medication carrier based on UiO-66 in response to this issue. Zinc phthalocyanine, a photosensitizer, is packed into this carrier (PS). Exogenous reactive oxygen species (ROS), which are capable of attacking several bacterial sites, were produced as a result of this PS. Conversely, PS has a greater capacity to swiftly and at a lower concentration render a variety of bacteria inactive. Lysis agents were also included to help the designed carrier pass through the cell wall, particularly in Gram-negative bacteria, as the cell wall is essential to the antimicrobial drug's efficacy. Zinc phthalocyanine was added to UiO-66 through an amination process.

Gram-positive *S. aureus*, MRSA, and *E. coli* were subjected to 670 nm light and darkness in an in vitro antibacterial activity test. In the presence of light, it was found that C1 transporter performed noticeably better than the other three at all concentrations for all three infections. Furthermore, the outcomes demonstrated that this medication delivery method might be a viable antibacterial agent carrier (Lv H. et al., 2020).

To sum up, when compared to alternative drug delivery methods, MOF nanoparticles offer a number of benefits, including chemical characteristics that facilitate modification and functioning as well as customizable structure and conformation (Li X. et al., 2018; Wu M.X. & Yang Y.W., 2017; Zhou T. et al., 2018). Furthermore, MOF alteration does not substantially change their appealing physicochemical characteristics. MOFs can likewise withstand high loading capacities due to their vast surface area and high porosity. Therefore, MOFs' biodegradability is guaranteed by the weak coordination interaction. For drug delivery applications, MOF nanoparticles (NPs) with the right size and surface characteristics are ideal since these attributes have a big influence on porosity, colloid stability, drug release patterns, and cellular absorption (He Z. and others, 2019; Wang H. and others, 2019).

## CHAPTER 2

### MATERIALS and METHODS

#### 2.1. Synthesis and Optimization Synthesized Nanoparticles

##### 2.1.1. ZIF-8 and 6-TG@ZIF-8 Nanoparticles

The synthesis of ZIF-8 nanoparticles was carried out with minor modifications to the method developed by Pan et al. (2011) (Pan et al., 2011). In this study, ZIF-8 nanoparticles were synthesized using the one-pot synthesis method with a  $Zn^{+2}$ :2-methylimidazole:  $H_2O$  molar ratio of 1:70:1238 (Kaur et al., 2017). According to the synthesis details, first  $Zn(NO_3)_2 \cdot 6H_2O$  (58.5 mg) was completely dissolved in 0.4 mL DI water. 2-methylimidazole (2-MeIM) (1.135 g) was completely dissolved in 4 mL DI water, 0.6 mL DMSO solution was added. Then, 2-MeIM solution was added onto the  $Zn(NO_3)_2 \cdot 6H_2O$  solution. After continuing the mixture at room conditions for 15 minutes, it was centrifuged at 13,500 rpm for 15 minutes to obtain white powder precipitates. The resulting nanoparticles were washed three times with 30:70 EtOH:  $H_2O$  and dried at room temperature.

The similar method described above was applied for the synthesis of 6-TG loaded ZIF-8 nanoparticle. Different concentrations (1.25, 2.5, 5 and 10 mg/mL) of 6-TG were dissolved in 0.6 mL DMSO and added to the 2-methylimidazole solution. Then, 2-MeIM solution was added onto the  $Zn(NO_3)_2 \cdot 6H_2O$  solution and the two solutions were mixed together to form a white solution. Other steps were continued such as ZIF-8 synthesis.

##### 2.1.2. UiO-66 and 6-TG@UiO-66 Nanoparticles

According to the synthesis details,  $ZrOCl_2 \cdot 8H_2O$  (1.6 g) and terephthalic acid (0.80 g) were dissolved in 30 mL DMF at room temperature. Formic acid (15.0 mL) was added to the mixture and stirred for 2 hours at 140°C using a reflux mechanism. The

resulting white precipitate was filtered after cooling to room temperature and washed once with 20 mL DMF and 50 mL acetone, and the collected white solids were dried at room temperature (Motegi et al., 2017)

For 6-TG loaded UiO-66 nanoparticle synthesis, pre-prepared UiO-66 (20 mg) was dispersed in 5 mL of DI water in the sonicator. Then, 1 mL of 6-TG aqueous solution at different concentrations (1.25, 2.5, 5 and 10 mg/mL) was added dropwise and mixed for 3 hours to form a white solution. The mixture was centrifuged at 13,500 rpm for 15 minutes to obtain white powder precipitates. The resulting nanoparticles were washed three times with DI water and dried at room temperature (Gao et al., 2018).

## **2.2. Characterization of Synthesized Nanoparticles**

### **2.2.1. Synthesis Yield of ZIF-8 and UiO-66 Nanoparticles**

At the end of the synthesis reaction, the theoretically required amounts of the synthesized nanoparticles were calculated using the gravimetric method. At the end of the synthesis reaction, the completely pure and dry product obtained will be experimentally clouded. The synthesis efficiency of the synthesized nanoparticles will be evaluated as a percentage according to the formula below.

$$\text{Synthesis Yield (\%)} = \frac{\text{Actual Yield}}{\text{Theoretical Yield}} \times 100$$

### **2.2.2. Determination of 6-TG Loading Effectiveness**

The loading efficiency of the 6-TG loaded samples to be synthesized will be determined using a UV-Visible Spectrophotometer. In the method, the drug loading capacity (%) will be calculated more accurately by creating a standard curve between the amount of 6-TG to be prepared in different amounts and the absorbance values measured at 349 nm, where the drug shows maximum absorption (Venna, Jasinski, & Carreon, 2010). After the nanoparticles are synthesized with 6-TG, they will be centrifuged, the concentration of the remaining drug in the medium and the amount bound to the nanoparticle will be determined and the loading capacity will be calculated.,

Environmental conditions (such as pH, temperature, time, speed) will be optimized to increase loading efficiency. Loading efficiency in % will be evaluated

according to the formula below.

$$\text{Loading Capacity (\%)} = \frac{\text{Amount of 6 - TG in nanoparticle}}{\text{Total amount of 6 - TG loaded}} \times 100$$

### 2.2.3. Structural Analysis

Particle size and zeta potential of ZIF-8, 6-TG@ZIF-8, UiO-66 and 6-TG@UiO-66 nanoparticles were studied by Dynamic Light Scattering Method (DLS) using Zetasizer Nano Z. The morphological properties of the nanoparticles will be examined by Scanning Electron Microscope (SEM) measurement and their sizes were compared with DLS results. Samples were imaged using the FEI QUANTA 250 FEG instrument with a 15 kV electron beam and 200 nm scale. Energy Dispersive X-ray Spectroscopy (EDX) was used to determine the elemental composition of the nanoparticles. The degree of crystallinity and impurity of the nanoparticles to be formed were determined by X-Ray Diffraction Device (XRD) measurement. Functional groups present in the nanoparticles were examined with Fourier Transform Infrared Analysis (FT-IR). Thermal properties of nanoparticles, such as thermal stability, were examined by Thermogravimetric Analysis (TGA).

## 2.3. Biocompatibility Tests of Synthesized Nanoparticles

### 2.3.1. Serum Protein Binding

The evaluation of the synthesized nanoparticles in terms of biocompatibility was evaluated by analyzing the possible binding of the nanoparticles to serum proteins. To determine protein binding rates to synthesized nanoparticles, the method applied by Choi et al. was modified and used (Choi et al., 2010). Fetal bovine serum (FBS) as (v/v): Synthesized nanoparticles were prepared in the ratios of 50:50, 60:40, 70:30, 80:20, 90:10, with a total volume of 500  $\mu$ L. The mixture was incubated for 2 hours at 37°C at 150 rpm and after incubation, phase separation was achieved by centrifuging the mixture at 14,000 rpm for 10 minutes. The supernatant was separated and the resulting pellet was washed twice with PBS buffer (pH 7.5) and the supernatant was obtained each time.

### 2.3.2. Hemolysis Analysis

Determining the hemolysis that synthesized nanoparticles can cause is necessary for the biocompatibility of nanoparticles. For this purpose, the method applied by Wu and his colleagues (Q. Wu et al., 2018) was modified and used. The blood taken into an EDTA tube was centrifuged at 1000 rpm for 10 minutes to obtain erythrocytes. After the erythrocytes were washed twice with PBS buffer and prepared, the erythrocytes were incubated with 2, 10 and 20  $\mu\text{g/mL}$  synthesized nanoparticles at  $37^\circ\text{C}$  for 6 hours, with a volume ratio of 1:1 (v/v). PBS was used as a negative control and Triton X-100 as a positive control. After each sample was centrifuged at 14,000 rpm for 10 minutes and nanoparticles were removed from the medium, hemoglobin was determined spectrophotometrically at 540 nm in the supernatant and the % hemolysis amount was calculated using the formula below.

$$\text{Hemolysis (\%)} = \frac{\text{Absorbance} - \text{Absorbance}_{\text{negative control (PBS)}}}{\text{Absorbance}_{\text{positive control (Triton X-100)}}} \times 100$$

### 2.4. Drug Release of 6-TG@ZIF-8 and 6-TG@UiO-66 Nanoparticles

Tumor cells have an acidic pH due to their rapid metabolism and anaerobic respiration. Additionally, ZIF-8 was shown to dissociate in acidic buffer by Sun et al. This promotes control of current drug release kinetics at pH 5.0, which mimics the internal environment of tumor cells; releases the drug. Additionally, release studies were carried out at physiological pH 7.4. Consequently, drug release kinetics were investigated in PBS at physiological temperature ( $37^\circ\text{C}$ ), pH = 7.4 and 5.0 with continuous shaking (3 mg of nanoparticle powder material was used in 1 mL). At regular intervals (0 to 96 hours), the centrifugation supernatant is removed and replaced with fresh PBS. PBS samples were collected each time. Absorbance measurement of supernatants was performed with a UV-Vis spectrophotometer (Shimadzu-UV-2550, Japan). To calculate the amount of drug released, the maximum absorbance peak given by the drug (for 6-TG at 349 nm) was taken as a reference.

## 2.5. Investigation of Antioxidant Activities

The antioxidant activities of the synthesized nanoparticles were examined using the DPPH scavenging test. First of all, solutions of the nanoparticles whose antioxidant activities were desired to be determined were prepared in methanol at different concentrations (1, 5, 10, 20, 50, 100 µg/mL). On the other hand, 100 µM solution was prepared by dissolving the DPPH radical in methanol. 2 mL of the prepared nanoparticle solutions was taken and placed in 50 ml glass amber beakers. Then, 2 mL of the prepared DPPH solution was added. Equal volumes of reagent and standard/sample were added to each glass amber beaker, making the final volume 4 ml. After the mixtures were vortexed, they were incubated at room temperature and in the dark for 30 minutes. The maximum absorbance values of the mixtures obtained were studied with a UV-VIS Spectrophotometer (Shimadzu 1601) against the reference solution at the wavelength where it gave maximum absorbance in the range of 515-528 nm. The antioxidant activity of the nanoparticles was calculated using the following equation.

$$\text{DPPH scavenging (\%)} = \frac{A_{\text{control}} - A_{\text{sample}}}{A_{\text{control}}} \times 100$$

$$A_{\text{sample}} = \text{absorbance of sample + DPPH}$$

$$A_{\text{control}} = \text{absorbance of DPPH}$$

## 2.6. Investigation of Antibacterial Activities

Nanoparticle's antibacterial activity was determined using the model Gram-negative bacteria (*E. coli*) and gram-positive bacteria (*S. aureus*) suspension with the counting-colony method according to the ASTM E2149 standard protocol. Then, *E. coli* was inoculated in nutrient agar (NA) and *S. aureus* was inoculated in tryptic soy agar (TSA). Next, the bacteria were incubated at 37°C. After incubation, bacteria colonies were picked off with a swab and mixed with 0.1% (w) peptone water to adjust concentration to the value of 0.5 in the McFarland ( $2.5 \times 10^7$  CFU/mL) standards scale. We kept our materials under UV for 15 minutes. Then, we named the flasks we chose to add our controls and substances and put 10 ml of PBS into each one. We added the substances that we kept under UV protection to the flasks we prepared, except for the PBS flasks for control. We took two eppendorfs and added 900 microliters of tryptic

soy agar and 100 microliters of our *E. coli* and *S. aureus* bacteria adjusted according to the standard separately. After vortex stage, we took 20 microliters from both eppendorfs and added them to the conical flasks. We closed the flasks tightly and put them in the shaker incubator for 1 day. It was shaken at 200 rpm at 37°C. We took our flasks out of the Shaker Incubator and placed them in the cabin where we would work. Then, we wrote the numbers 0, 10 to the power of 2, and 10 to the power of 4 on our petri dishes with the medium prepared for *E. coli* and *S. aureus*, and divided them into threes. For each solution we prepared, we arranged 4 eppendorfs and added 900 microliters of peptone water into each eppendorf. We took a 100 microliter of sample from the solution, and after planting it in the petri dish marked 0 without any dilution, we took another 100 microliters from the solution, added it to the eppendorf, vortexed it, and continued by diluting it to 10 to the 2nd and 10th to the 4th respectively. After this stage, we carried out the planting process in our petri dishes of 2 to the 10th power and 4 to the 10th power. We performed the seeding process in the same way for each solution. Finally, we spread the bacteria with a Dirigalski spatula at the flame, placed them in a 37°C incubator, waited for colony formation for 1 day, and counted them in cfu/ml. In antibacterial activity calculation, inoculum solution (without containing any nanoparticles) was used as control. The antibacterial activity test was repeated three times (n=3).

### **2.6.1. Preparation of Nutrient Agar Medium**

To prepare this medium, 6.4 grams of nutrient broth and 12 grams of agar were weighed and dissolved in 800 ml of distilled water and then sterilized in an autoclave. The autoclave outlet was allowed to cool to a temperature that would not gel, and then it was poured into petri dishes in the biosafety cabinet.

### **2.6.2. Preparation of Tryptic Agar Medium**

To prepare this medium, 24 grams of tryptic soy broth and 12 grams of agar were weighed and dissolved in 800 ml of distilled water and then sterilized in an autoclave. The autoclave outlet was allowed to cool to a temperature that would not gel, and then it was poured into petri dishes in the biosafety cabinet.

## CHAPTER 3

### RESULTS AND DISCUSSION

#### 3.1. Synthesis and Optimization Synthesized Nanoparticles

Optimization studies were carried out on the synthesis of ZIF-8, 6-TG@ZIF-8, UiO-66 and 6-TG@UiO-66 nanoparticles, which were targeted to be synthesized and optimization results are stated in the structural results section.

#### 3.2. Characterization of Synthesized Nanoparticles

##### 3.2.1. Synthesis Yield of ZIF-8 and UiO-66 Nanoparticles

$$\text{Yield (\%)} = \frac{\text{Actual Yield}}{\text{Theoretical Yield}} \times 100$$

In this study, ZIF-8 was synthesized with a  $\text{Zn}^{+2}$ :2-methylimidazole:  $\text{H}_2\text{O}$  molar ratio of 1:70:1238. According to this synthesis method, the synthesis was carried out using 0.197 mmol  $\text{Zn}(\text{NO}_3)_2 \cdot 6\text{H}_2\text{O}$  and 0.394 mmol 2-methylimidazole (2-MeIM). 0.160 mmol of ZIF-8 nanoparticles was obtained. It was found that ZIF-8 nanoparticles were synthesized with 81.2% efficiency when calculated using the above formula.

In this study, UiO-66 was synthesized as 5.0 mmol  $\text{ZrOCl}_2 \cdot 8\text{H}_2\text{O}$  and 4.8 mmol terephthalic acid. When calculated using the above formula, it was found that UiO-66 nanoparticles were synthesized with 81.4% yield.

##### 3.2.2. Drug Loading Capacity

UV-Vis spectrophotometer was also used in 6-TG loading efficiency studies. After incubation with 6-TG, the nanoparticles were centrifuged and the absorbance measurement of the resulting supernatant was taken with a Shimadzu-UV-2550UV-Vis spectrophotometer. To calculate the amount of unloaded drug, the maximum absorbance peak of the drug at 349 nm was taken as a reference.

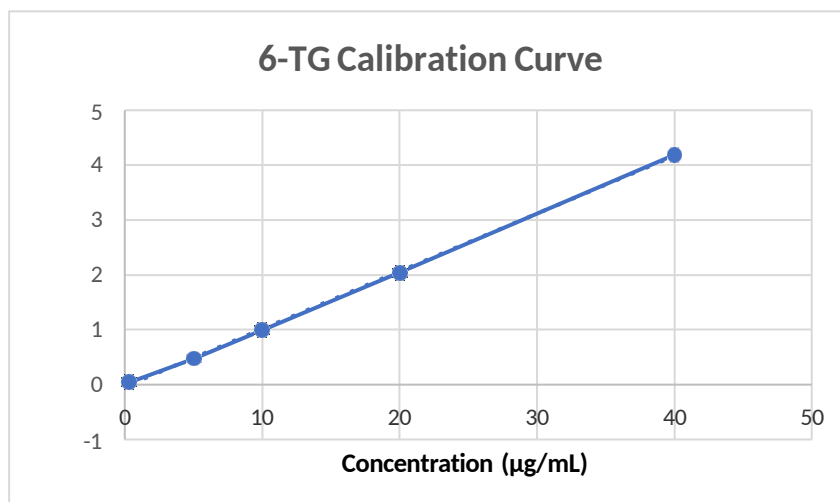


Figure 3.1. Calibration Curve of 6-TG

The loading efficiencies of 6-TG@ZIF-8 (1.25 mg/mL, 2.5 mg/mL, 5 mg/mL, 10 mg/mL) nanoparticles at different concentrations were calculated and given in the Table 3.1.

Table 3.1. 6-TG Loading Capacity of 6-TG@ZIF-8 Nanoparticles

Nanoparticles	Yield %
6-TG@ZIF-8 (10 mg/mL)	64%
6-TG@ZIF-8 (5 mg/mL)	67%
6-TG@ZIF-8 (2,5 mg/mL)	92%
6-TG@ZIF-8 (1,25 mg/mL)	46%

The loading efficiencies of 6-TG@UiO-66 (1.25 mg/mL, 2.5 mg/mL, 5 mg/mL, 10 mg/mL) nanoparticles at different concentrations were calculated and given in the Table 3.2.

Table 3.2. 6-TG Loading Capacity of 6-TG@UiO-66 Nanoparticles

Nanoparticles	Yield %
6-TG@UiO-66 (10 mg/mL)	78%
6-TG@UiO-66 (5 mg/mL)	82%
6-TG@ UiO-6 (2,5 mg/mL)	94%
6-TG@UiO-66 (1,25 mg/mL)	67%

### 3.2.3. Structural Analysis

#### 3.2.3.1. Scanning Electron Microscopy

##### 3.2.3.1.1. ZIF-8 and 6-TG@ZIF-8 Nanoparticles

Scanning electron microscope SEM images of the nanoparticles were taken to observe the radius and morphology of the ZIF-8 and 6-TG@ZIF-8 nanoparticles obtained at the end of the reaction (Fig 3. 2). The obtained SEM images showed that ZIF-8 crystals consisted of homogeneously dispersed rhombic dodecahedral-shaped nanoparticles (Hoop et al., 2018).

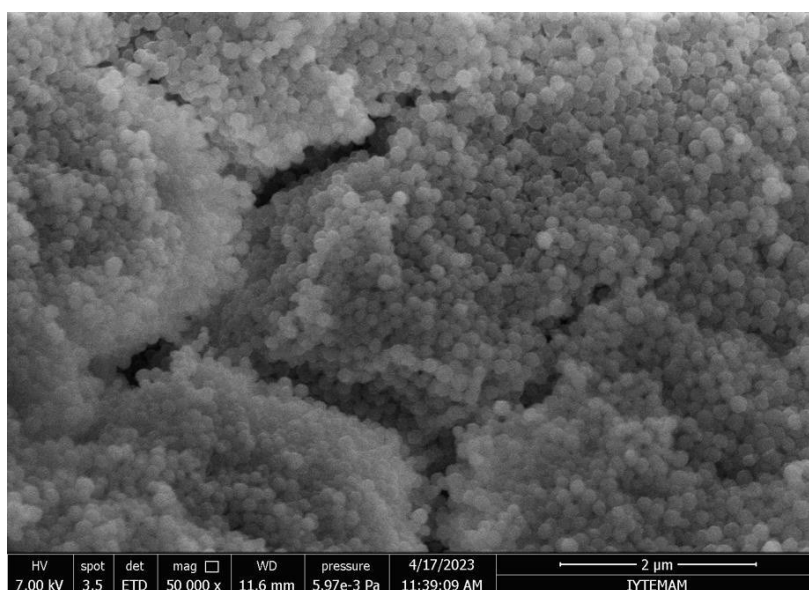


Figure 3.2. SEM micrographs of ZIF-8

The size of the obtained ZIF-8 nanoparticles is  $124 \pm 45$  nm and the size of 6-TG@ZIF-8 (1,25 mg/mL, 2,5 mg/mL, 5 mg/mL) nanoparticles is  $219 \pm 15$ ,  $251 \pm 15$ ,  $233 \pm 1$  nm, found respectively. Diameter could not be calculated because the morphology of 6-TG@ZIF-8 (10 mg/mL) nanoparticles was disrupted (Fig 3. 3).

Zheng (2016) encapsulated the anticancer drug doxorubicin and Kaur (2017) the drug 6-mercaptopurine into ZIF-8 nanocrystal and observed an increase in particle diameters at different rates. Chowdhuri et al. (2016) and Karakeçili (2019), the vancomycin antibiotic was encapsulated in ZIF-8 nanocrystals and no significant change

in particle size was observed. When all these studies were evaluated, it was concluded that the change in nanocrystal diameters after the encapsulation of molecules may vary depending on the encapsulated molecule and its interaction with the nanocrystal (Chowdhuri et al., 2016; Karakeçili et al., 2019; Kaur et al., 2017).

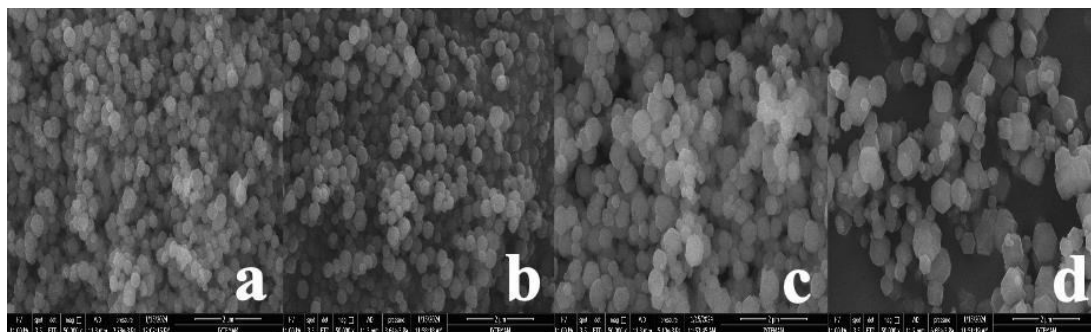


Figure 3.3. SEM micrographs of a) 6-TG@ZIF-8 (1,25 mg/mL) b) 6-TG@ZIF-8 (2,5 mg/mL) c) 6-TG@ZIF-8 (5 mg/mL) d) 6-TG@ZIF-8 (10 mg/mL)

An increase in diameter was observed when we encapsulated 6-TG into ZIF-8 nanocrystal. The loading efficiencies of the synthesized nanoparticles and the nanoparticle diameters calculated from Scanning electron microscope (SEM) images were evaluated. Considering the high loading efficiency and small nanoparticle radius, the concentration of suitable nanoparticles for our studies was decided to be 6-TG@ZIF-8 (5 mg/mL) (Fig 3. 4).

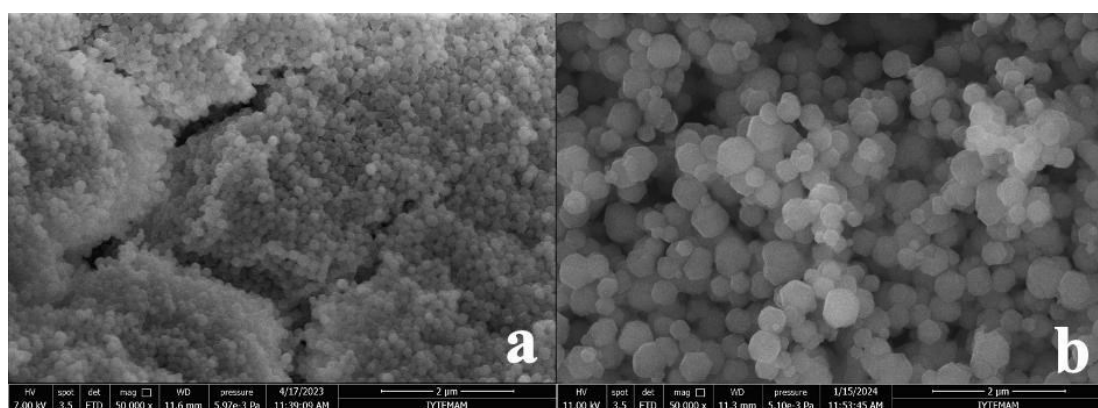


Figure 3.4. SEM micrographs of a) ZIF-8 and b) 6-TG@ZIF-8 (5 mg/mL)

### 3.2.3.1.2. UiO-66 and 6-TG@UiO-66 Nanoparticles

Scanning electron microscope (SEM) images of the nanoparticles were taken to observe the radius and morphology of the UiO-66 and 6-TG@UiO-66 nanoparticles obtained at the end of the reaction (Fig 3.5). The obtained SEM images showed that UiO-66 crystals consisted of homogeneously dispersed nanoparticles (Hoop et al., 2018).

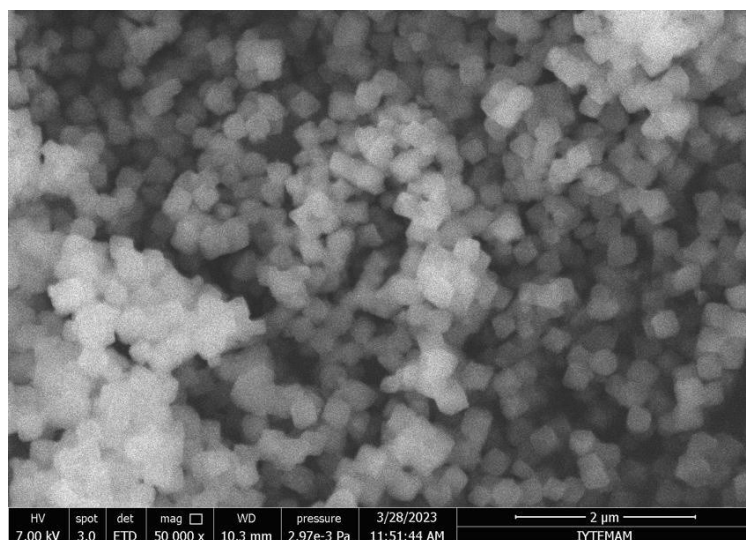


Figure 3.5. SEM micrographs of UiO-66

The size of the obtained UiO-66 nanoparticles is  $271 \pm 30$  nm and the size of 6-TG@UiO-66 (1.25 mg/mL, 2.5 mg/mL, 5 mg/mL) nanoparticles is 372, 370, 362 nm, respectively was found. Diameter could not be calculated because the morphology of 6-TG@UiO-66 (10 mg/mL) nanoparticles was disrupted (Fig 3.6).

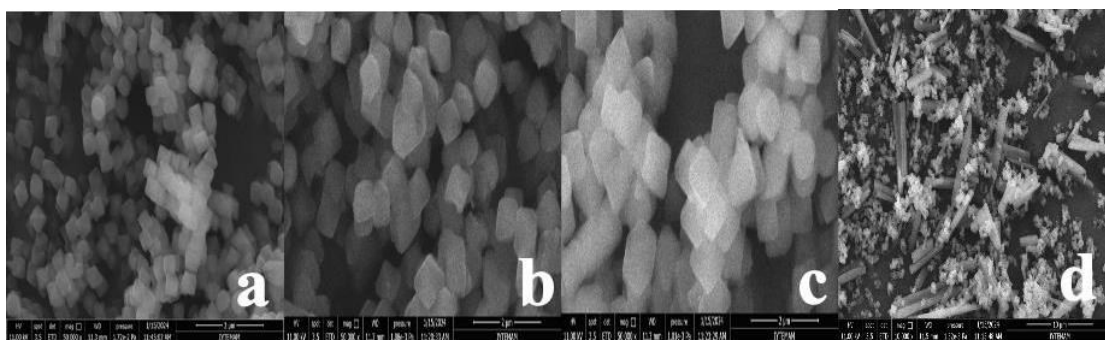


Figure 3.6. SEM micrographs of a) 6-TG@UiO-66 (1,25 mg/mL) b) 6-TG@UiO-66 (2,5 mg/mL) c) 6-TG@UiO-66 (5 mg/mL) d) 6-TG@UiO-66 (10 mg/mL)

An increase in diameter was observed when we encapsulated 6-TG into the UiO-66 nanoparticle. The loading efficiencies of the synthesized nanoparticles and the nanoparticle diameters calculated from Scanning electron microscope (SEM) images were evaluated. Considering the high loading efficiency and small nanoparticle radius, the concentration of suitable nanoparticles for our studies was decided to be 6-TG@UiO-66 (5 mg/mL) (Fig 3.7).

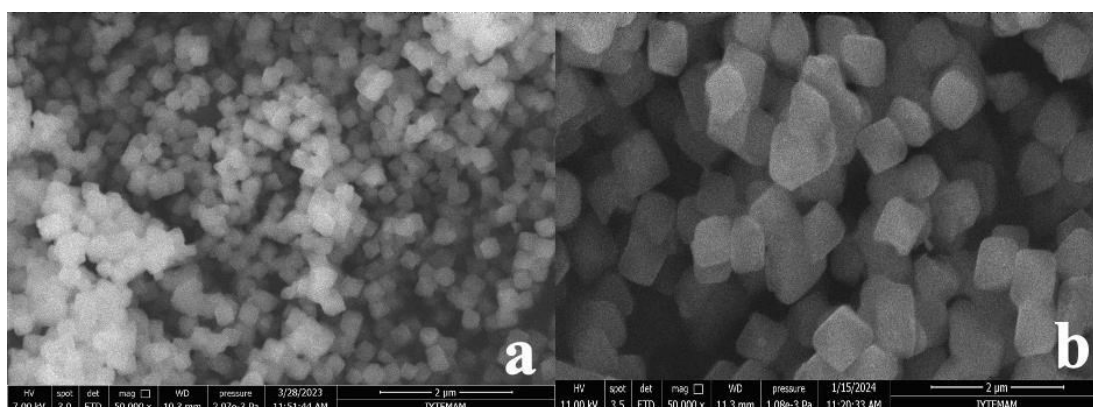


Figure 3.7. SEM micrographs of a) UiO-66 and b) 6-TG@UiO-66 (5 mg/mL)

### 3.2.3.2. Energy Dispersive X-Ray Spectroscopy (EDX)

#### 3.2.3.2.1. ZIF-8 and 6-TG@ZIF-8 Nanoparticles

The atomic percentages of ZIF-8 and 6-TG@ZIF-8 nanoparticles are varied using the EDX method (Table 3.3). It is compatible with the current atomically occurring closed formula of ZIF-8,  $C_8H_{10}N_4Zn$ . As for the geographical appearance of 6-TG@ZIF-8 and ZIF-8 nanoparticles, it is observed that in the atomic percentage case of 6-TG@ZIF8, the S element from 6-TG is added and the percentage of the total proportions of the Zn element present increases.

Table 3.3. EDX curves and elemental compositions of ZIF-8 and 6-TG@ZIF-8 (5mg/mL)

6-TG@ZIF-8		
Element	Wt %	Atomic %
O	13,08	0,03
Zn	35,81	9,88

6-TG@ZIF-8		
Element	Wt %	Atomic %
C	41,9	62,92
N	20,02	26,01
O	13,08	0,03
Zn	35,81	9,88
S	2,05	1,15

### 3.2.3.2.2. UiO-66 and 6-TG@UiO-66 Nanoparticles

Atomic percentages of UiO-66 and 6-TG@UiO-66 nanoparticles were found using the EDX method (Table 3.4). The atomic percentage distribution of UiO-66 is compatible with the closed formula  $Zr_6O_4(OH)_4(RCOO)_{12}$ . When the distribution of 6-TG@ZIF-8 and UiO-66 nanoparticles is compared, it is observed that in the 6-TG@ZIF-8 atomic percentage distribution, the S element from 6-TG is added and the percentage of the Zr element present decreases compared to the total ratio.

Table 3.4. EDX curves and elemental compositions of ZIF-8 and 6-TG@ZIF-8 (5 mg/mL)

6-TG@ZIF-8		
Element	Wt %	Atomic %
O	33,73	77,25
Zr	62,67	22,75

6-TG@ZIF-8		
Element	Wt %	Atomic %
C	30,98	41,25
N	33,73	38,51
O	13,08	13,07
Zr	12,10	2,12
S	10,11	5,04

### 3.2.3.3. Fourier Transform Infrared Analysis Energy Dispersive X-Ray (FT-IR)

#### 3.2.3.3.1. ZIF-8 and 6-TG@ZIF-8 Nanoparticles

The functional groups present in ZIF-8 and 6-TG@ZIF-8 were determined by Fourier Transform Infrared Analysis (FT-IR). In the spectrum corresponding to ZIF-8, bands at 3135 and 2928  $cm^{-1}$  were observed for the aromatic C–H bond and aliphatic C–H bond of imidazole, respectively. The bands at 1606  $cm^{-1}$  and 1580  $cm^{-1}$  were observed for C–C bond and C–N bond, respectively. C–N absorption bands are located in the range of 1100–1400  $cm^{-1}$ . The absorption band at 421  $cm^{-1}$  is associated with the Zn–N stretching mode. This spectrum is consistent with FTIR measurements found in the literature by Park et al. (Park, Ni, Côté, Choi, Huang, Uribe-Romo, Chae, O’Keeffe et al., 2006) (Fig 3.8).

Various bands were observed for 6-TG. FTIR spectrum analysis for the 6-TG@ZIF-8 system does not undoubtedly indicate the adsorption of 6-TG to ZIF-8, but the detection of characteristic bands for both ZIF-8 and 6-TG indicates the presence of both compounds (Fig 3.8).

When we look at the studies in the literature, a study conducted by coating 6-MP@ZIF-8 nanoparticles with 6-mercaptopurine with ZIF-8 was examined. When the spectra obtained for ZIF-8 and 6-MP@ZIF-8 nanoparticles were compared, it was noticed that the spectra of the two samples showed very high similarities. However, due to encapsulation within the ZIF-8 framework, the characteristic peaks of 6-MP appeared to be masked. As in this study, it was observed that the FTIR spectrum of 6-TG@ZIF-8 nanoparticles was similar to ZIF-8 nanoparticles and the characteristic peaks of 6-TG were suppressed by the peaks of ZIF-8 nanoparticles. This result is associated with the encapsulation of 6-TG into ZIF-8 (Fig 3.8).

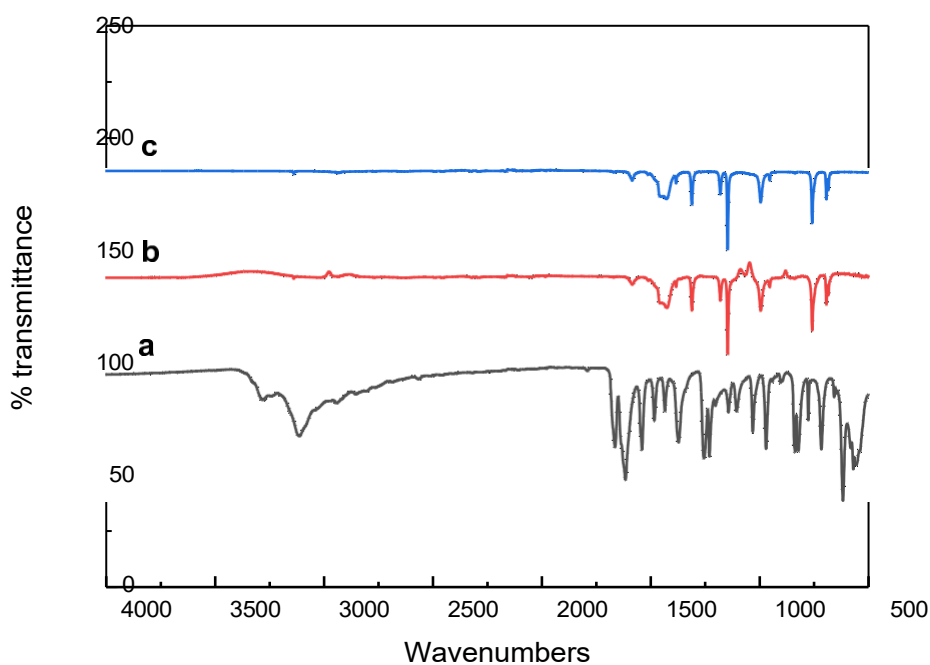


Figure 3.8. FTIR spectra of a) 6-TG, b) ZIF-8 and c) 6-TG@ZIF-8 (5 mg/mL)

### 3.2.3.3.2. UiO-66 and 6-TG@UiO-66 Nanoparticles

Strong bands of O-C-O asymmetric and symmetric stretching in UiO-66 (Zr), BDC ligand, can be found at 1597 and 1406 cm<sup>-1</sup>. The weak band at 1504 cm<sup>-1</sup> shows the C=C vibration of the benzene ring. The peaks at 808, 746 and 658 cm<sup>-1</sup> are combined

with C-H vibration, C=C stretching, OH bending and O-C-O bending in the BDC ligand. In addition, a band related to the C=O asymmetric stretching of DMF can be shown at 1655 cm, which means that DMF is located in the pores. However, the fact that no absorption band associated with the carboxylate vibration bands of the free BDC ligand was observed at 1685 cm<sup>-1</sup> shows that all carboxylates are bound to zirconium ions. These results were found to be consistent with the literature.

Various bands were observed for 6-TG. FTIR spectrum analysis for the 6-TG@UiO-66 system does not undoubtedly indicate the adsorption of 6-TG to UiO-66, but the detection of characteristic bands for both UiO-66 and 6-TG indicates the presence of both compounds (Fig 3.9).

When we look at the studies in the literature, a study conducted by coating Gin@UiO-66 nanoparticles with Gingerol and UiO-66 was examined. When the spectra obtained for UiO-66 and Gin@UiO-66 nanoparticles were compared, it was noticed that the spectra of the two samples showed very high similarities. However, due to encapsulation within the ZIF-8 framework, the characteristic peaks of 6-MP appeared to be masked (Kazazi et al., 2023). As in this study, it was observed that the FTIR spectrum of 6-TG@ UiO-66 nanoparticles was similar to that of UiO-66 nanoparticles and the characteristic peaks of 6-TG were suppressed by the peaks of UiO-66 nanoparticles. This result is associated with the encapsulation of 6-TG into UiO-66 (Fig 3.9).

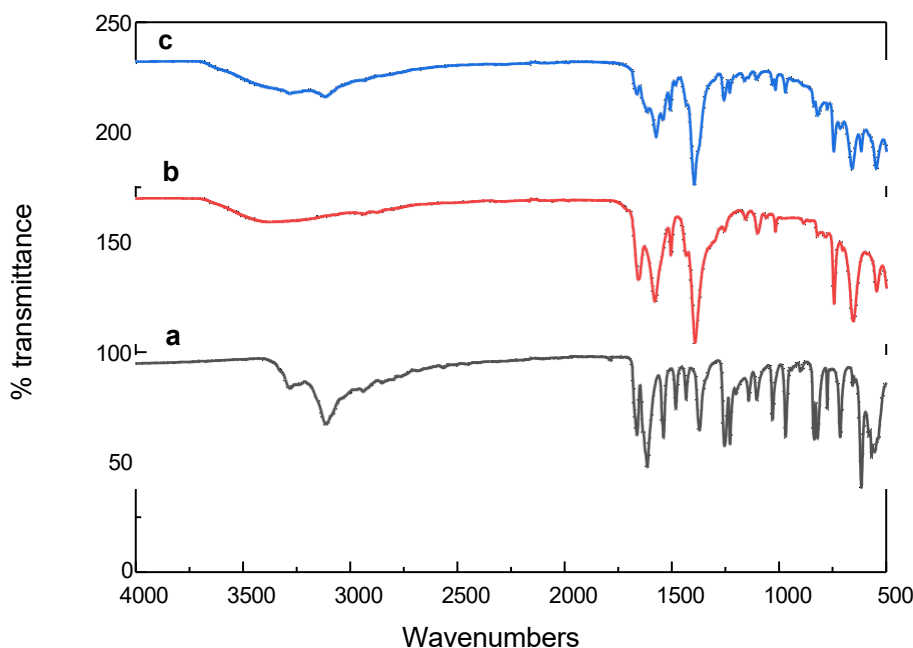


Figure 3.9. FTIR spectra of a) 6-TG, b) UiO-66 and c) 6-TG@UiO-66 (5 mg/mL)

### 3.2.3.4. X-Ray Diffraction Device (XRD)

#### 3.2.3.4.1. ZIF-8 and 6-TG@ZIF-8 Nanoparticles

When we look at the studies in the literature, the published XRD pattern shows that the product obtained with ZIF-8 nanoparticles is pure phase ZIF-8 material. The observed peak broadening is in agreement with the sample XRD pattern indicating the formation of nano-sized crystals and confirms the sodalite structure. Pure phase ZIF-8 nanoparticle synthesis appears to occur as shown by X-ray diffraction (XRD) patterns (Figure 24). Patterns formed by the ordered porous structure of ZIF-8 nanoparticles between  $2\theta$  values of 5 and  $40^\circ$  can be observed, and the observed peak broadening indicates the formation of nano-sized crystals. Relative intensities and sharp peaks in the diffraction pattern of ZIF-8 at prominent peak positions of  $2\theta=7.11^\circ$ ,  $12.5^\circ$ ,  $17.75^\circ$ , and  $26.4^\circ$  including 011, 002, 112, 022, 013, and 222. The typical structure and identified peaks of ZIF-8 are in agreement with the literature (Cravillon and et.al., 2009; Park, Ni, Côté, Choi, Huang, Uribe-Romo, Chae, O’Keeffe, and et. al., 2006).

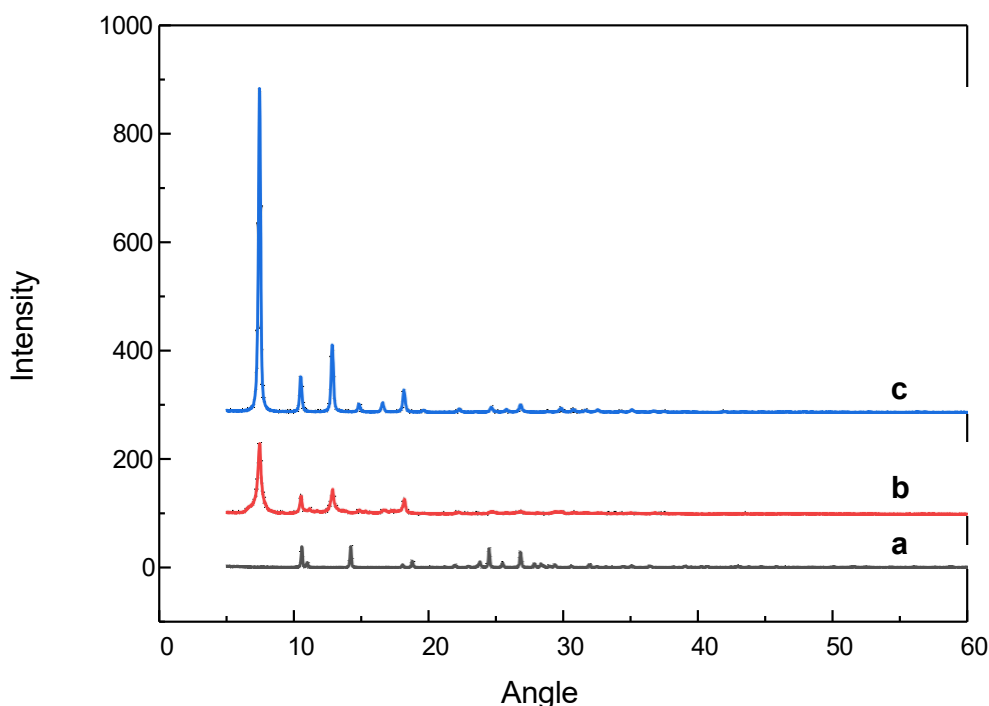


Figure 3.10. XRD patterns of a) 6-TG, b) ZIF-8 and c) 6-TG@ZIF-8 (5 mg/mL)

When we look at the studies in the literature, it has been observed that the powder XRD pattern does not show a significant change in the crystal structure of 6-MP@ZIF-8 nanoparticles compared to ZIF-8 (Q. Wu et al., 2018). This study shows that the crystallinity of ZIF-8 does not change with the encapsulation of 6-TG drug into ZIF-8 nanoparticles and the integrity of the MOF is well preserved (Fig 3.10).

### 3.2.3.4.2. UiO-66 and 6-TG@UiO-66 Nanoparticles

X-ray powder diffraction method was used to measure the phases of the synthesized samples. Figure 1 shows the XRD pattern of a typical synthesized sample. The formation of the UiO-66 structure is confirmed by the excellent agreement of the experimental XRD model with the theoretical powder model. The diffraction peak positions and relative diffraction intensities for UiO-66 were found to be in agreement with the standard data, thus proving that the synthesized sample was UiO-66. Meanwhile, the agreement between the experimental and simulated XRD patterns demonstrated the phase purity of the synthesized UiO-66 product.

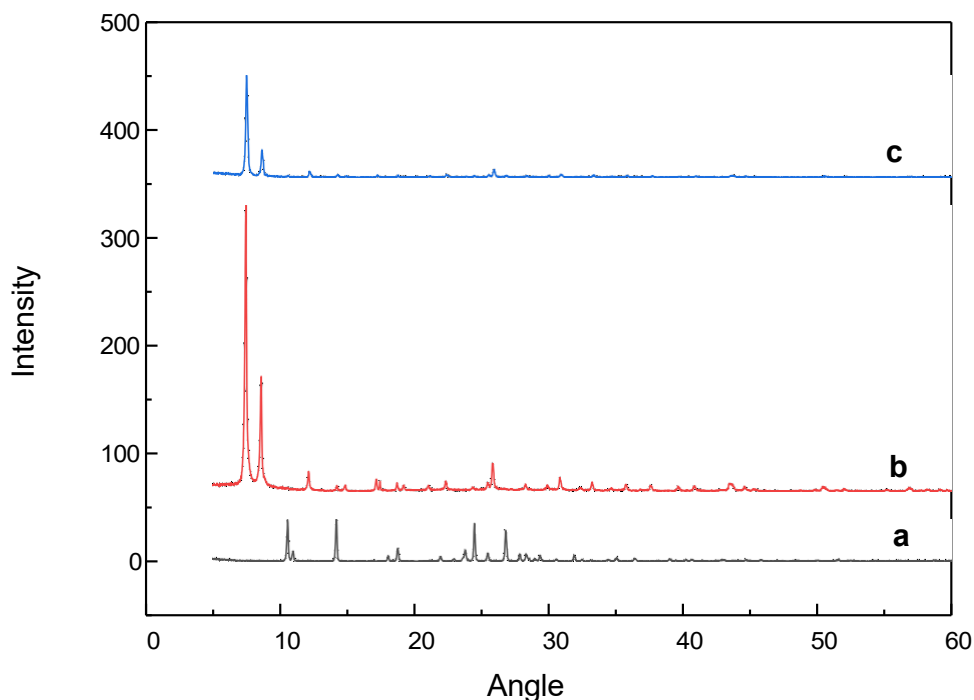


Figure 3.11. XRD patterns of a) 6-TG, b) UiO-66 and c) 6-TG@UiO-66 (5 mg/mL)

When we look at the studies in the literature, it has been observed that the powder XRD pattern does not show a significant change in the crystal structure of ICG@UiO-66 nanoparticles compared to UiO (Kazazi et al., 2023). XRD analysis of the

nanoparticle as in this study shows unchanged lattice parameters and similar strong diffraction peaks for UiO-66 before and after 6-TG loading. This shows that the integrity of the MOF is well preserved (Fig 3.11).

### 3.2.3.5. Dynamic Light Scattering Method (DLS) and Zeta Potential

#### 3.2.3.5.1. ZIF-8 and 6-TG@ZIF-8 Nanoparticles

The hydrodynamic radii of the synthesized nanoparticles were examined by dynamic light scattering (DLS). The resulting nanoparticles were well dispersed in ethanol to form a stable suspension. ZIF-8 and 6-TG@ZIF-8 and the average particle sizes of the nanoparticles are shown in Table 3.5. When the radii found are examined, it is seen that they are similar to the SEM images. According to the results obtained from SEM images, an increase in diameter occurred when we encapsulated 6-TG into the ZIF-8 nanoparticle. A similar situation is observed in the results obtained with DLS.

The zeta potential of nanoparticles is an important factor for the cellular retention rate in in vitro applications. Zeta potential is an important indicator of the stability of colloidal dispersions. Colloids with high zeta potential (negative or positive) are electrically stabilized, while colloids with low zeta potential tend to coagulate or clump. To prepare a reasonable dispersion without agglomeration in any colloidal structure, particles must have surface charges and therefore understanding surface charges is critical to decide the adsorption of these particles to a surface or affinity to the targeted site.

Zeta potential sizes of nanoparticles are shown in Table 3.5. This change in zeta potential can be attributed to the encapsulation of 6-TG. The difference in zeta potential also provided evidence for the success of nanoparticle synthesis. These positive values for electronegativity will increase cellular uptake.

Table 3.5. Hydrodynamic radius and zeta potentials of ZIF-8 and 6-TG@ZIF-8 (5 mg/mL)

	Hydrodynamic Radius (nm)	Zeta Potential (mV)
<b>ZIF-8</b>	461.0	26.77
<b>6-TG@ZIF-8 (5 mg/mL)</b>	514,7	32.85

### 3.2.3.5.2. UiO-66 and 6-TG@UiO-66 Nanoparticles

The hydrodynamic radii of the synthesized nanoparticles were examined by dynamic light scattering (DLS). The resulting nanoparticles were well dispersed in ethanol to form a stable suspension. The average particle sizes of UiO-66 and 6-TG@UiO-66 nanoparticles are shown in Table 3.6. When the radii found are examined, it is seen that they are similar to the SEM images. According to the results obtained from SEM images, an increase in diameter was observed when we encapsulated 6-TG into the UiO-66 nanoparticle. A similar situation is observed in the results obtained with DLS.

Zeta potential sizes of nanoparticles are shown in Table 3. This change in zeta potential can be attributed to the encapsulation of 6-TG. The difference in zeta potential also provided evidence for the success of nanoparticle synthesis. These positive values for electronegativity will increase cellular uptake.

Table 3.6. Hydrodynamic radius and zeta potentials of UiO-66 and 6-TG@UiO-66 (5 mg/mL)

	Hydrodynamic Radius (nm)	Zeta Potential (mV)
UiO-66	902.3	18.91
6-TG@UiO-66 (5 mg/mL)	977.2	9.25

### 3.2.3.6. Thermogravimetric Analysis (TGA)

#### 3.2.3.6.1. ZIF-8 and 6-TG@ZIF-8 Nanoparticles

The 6-TG TGA graph shows a slow drop in weight with rising temperatures. Up to a particular temperature range, the mass is initially quite constant. The mass then gradually decreases as the temperature rises, signifying the breakdown of 6-TG molecules. Typically, the curve displays a single, broad peak that represents the 6-TG breakdown process. At lower temperatures, the ZIF-8 TGA graph shows minimal weight loss and impressive thermal stability. The material's stability is first indicated by a flat baseline. A fast and severe mass reduction at higher temperatures is seen, indicating ZIF-8 breakdown. Up to a certain temperature, ZIF-8 exhibits good thermal stability; beyond that, it decomposes quickly. The 6-TG@ZIF-8 nanoparticle TGA graph

combines 6-TG and ZIF-8 properties.

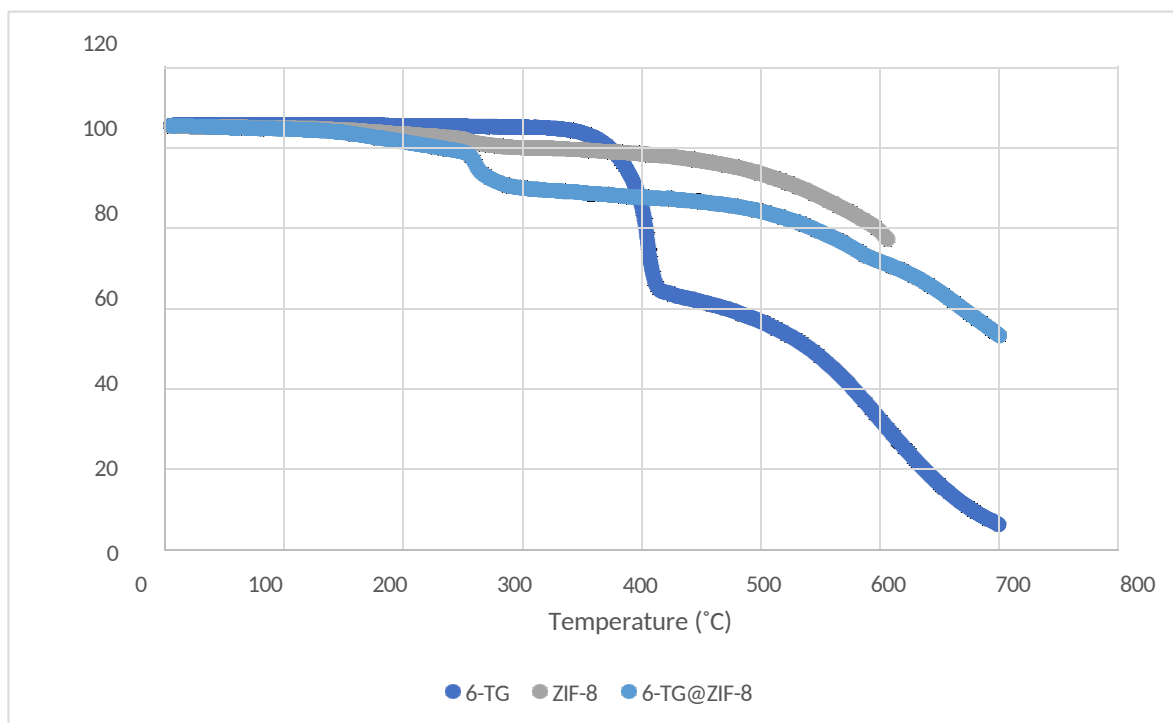


Figure 3.12. TGA graphs of 6-TG, ZIF-8 and 6-TG@ZIF-8 (5 mg/mL)

There might be a steady mass at first, akin to 6-TG, and then a slow decline in mass that corresponds to the breakdown of 6-TG molecules. The graph may also display ZIF-8 characteristics, such as a plateau in stability at high temperatures or an abrupt drop in weight that corresponds to the ZIF-8 component breaking down. The TGA curve for 6-TG@ZIF-8 nanoparticles may show several weight loss steps, plateaus, or a combination of both 6-TG and ZIF-8 thermal behaviors, depending on the composition and interaction between 6-TG and ZIF-8.

### 3.2.3.6.2. UiO-66 and 6-TG@UiO-66 Nanoparticles

Weight usually decreases gradually as temperature rises on the TGA graph for 6-TG. As the temperature rises at first, there isn't much weight loss, which suggests that the 6-TG molecule is stable. The steady loss of mass with increasing temperature is indicative of the breakdown of 6-TG molecules. The curve frequently shows a single broad peak, which represents the 6-TG breakdown process.

At lower temperatures, the TGA graph of UiO-66 usually shows minor weight loss and great thermal stability. At first, a level baseline shows that the UiO-66

architecture is stable. The mass decreases abruptly and sharply at increasing temperatures, suggesting that UiO-66 is breaking down. Up to a specific temperature threshold, UiO-66 demonstrates good thermal stability; beyond this point, breakdown proceeds rapidly. Features of both 6-TG and UiO-66 are combined in the TGA graph for 6-TG@UiO-66 nanoparticles.

There might be a steady mass at first, close to 6-TG, and then a slow decline in mass that corresponds to the breakdown of 6-TG molecules. Furthermore, the graph can show UiO-66 features like a stability plateau at high temperatures or an abrupt weight decrease that denotes the breakdown of the UiO-66 structure. The TGA curve for 6-TG@UiO-66 nanoparticles may show several weight loss stages, plateaus, or a combination of both 6-TG and UiO-66 thermal behaviors, depending on the composition and interaction between 6-TG and UiO-66.

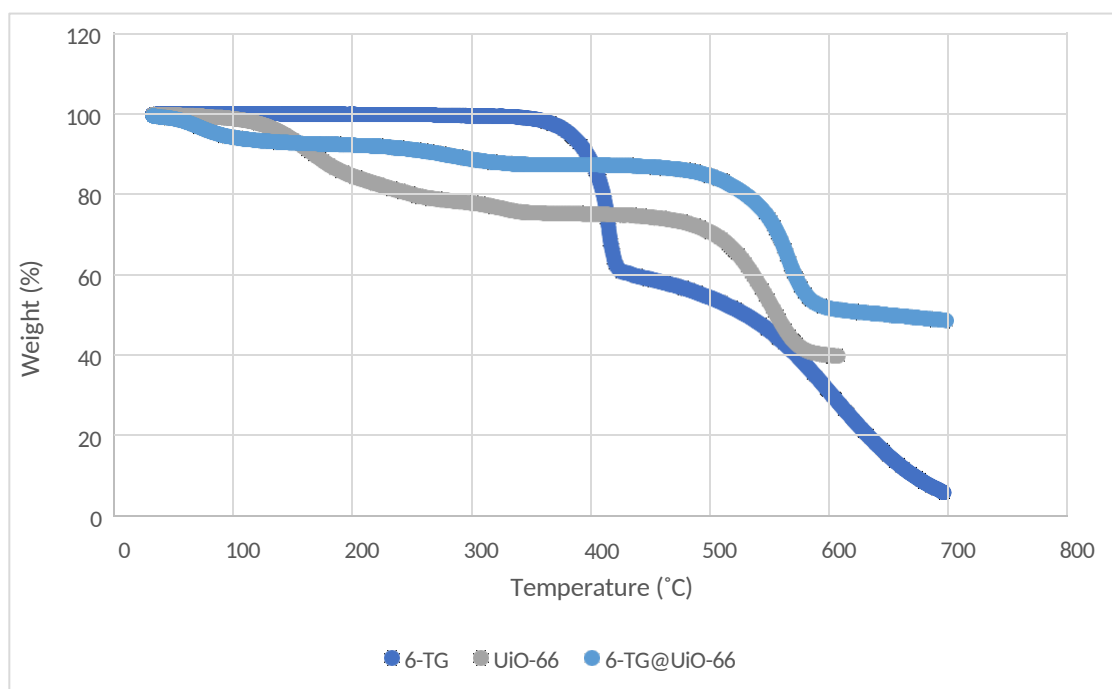


Figure 3.13. TGA graphs of 6-TG, UiO-66 and 6-TG@UiO-66 (5 mg/mL)

### 3.3. Biocompatibility Tests of Synthesized Nanoparticles

#### 3.3.1. Serum Protein Binding

Although protein binding to nanostructures is not a fully explained mechanism, protein binding changes the charge of the nanoparticle (Aggarwal et al., 2009). It is stated in the literature that the size, surface charge, solubility, surface modifications and shape

of the nanoparticle are effective factors in binding to plasma proteins.

The binding rate of the synthesized nanoparticles to serum proteins was investigated to demonstrate the biocompatibility of the nanoparticles. The amount of binding to serum proteins was calculated by measuring FBS (as serum protein equivalent) in the presence of nanoparticles after two hours of incubation at 37°C. Since it is known that drugs taken intravenously are eliminated from the body in approximately 2 hours, the duration was set as 2 hours. Additionally, incubation was carried out at 37°C, which is body temperature. Since the amount of serum protein may vary from person to person, serum: nanoparticle ratios (50:50, 60:40, 80:20, 90:10) were tested.

### 3.3.1.1. ZIF-8 and 6-TG@ZIF-8 Nanoparticles

The binding percentages of 6-TG, ZIF-8 and 6-TG@ZIF-8 nanoparticles to the obtained serum proteins are summarized in Table 3.7. When the results were examined, it was seen that the binding percentage of the synthesized nanoparticles to serum proteins was below 20.

Table 3.7. Protein Binding (%) of 6-TG, ZIF-8 and 6-TG@ZIF-8 (5 mg/mL)

$V_{\text{serum}}:V_{\text{nanoparticle}}$	Protein Binding (%)		
	6-TG	ZIF-8	6-TG@ZIF-8
<b>50:50</b>	2,25	4,09	4,98
<b>60:40</b>	7,75	15,07	2,82
<b>70:30</b>	11,72	10,34	0,38
<b>80:20</b>	5,64	9,10	2,83
<b>90:10</b>	4,87	6,45	3,56

### 3.3.1.2. UiO-66 and 6-TG@UiO-66 Nanoparticles

The binding percentages of nanoparticles of 6-TG, UiO-66 and 6-TG@UiO-66 nanoparticles to the obtained serum proteins are summarized in Table 3.8. When the results were examined, it was seen that the binding percentage of the synthesized nanoparticles to serum proteins was below 20.

Table 3.8. Protein Binding (%) of 6-TG, UiO-66 and 6-TG@UiO-66 (5 mg/mL)

$V_{\text{serum}}:V_{\text{nanoparticle}}$	Protein Binding (%)		
	6-TG	UiO-66	6-TG@UiO-66
50:50	2,25	3,00	1,7
60:40	7,75	4,80	4,47
70:30	11,72	9,53	7,02
80:20	5,64	1,22	6,21
90:10	4,87	12,31	5,41

### 3.3.2. Hemolysis

The percentage of synthesized nanoparticles in erythrocyte cells in the blood was investigated. Erythrocytes, also known as red blood cells, make up 48% of the blood. Erythrocyte-MOF interaction is essential for studying hemoglobin release (known as hemolysis) (Ferdous and Nemmar, 2020). When Triton X-100 was used as a positive control, it was observed that there was hemolysis at a high level at the beginning of the experiment, and there was no hemolysis in the negative control tubes.

#### 3.3.2.1. ZIF-8 and 6-TG@ZIF-8 Nanoparticles

2  $\mu\text{g/mL}$ , 10  $\mu\text{g/mL}$  and 20  $\mu\text{g/mL}$  as hemolysis rates of 6-TG, ZIF-8 and 6-TG@ZIF-8 nanoparticles were determined. The fact that these values are below 5% supports the biocompatibility of nanoparticles (Fig 3.14).

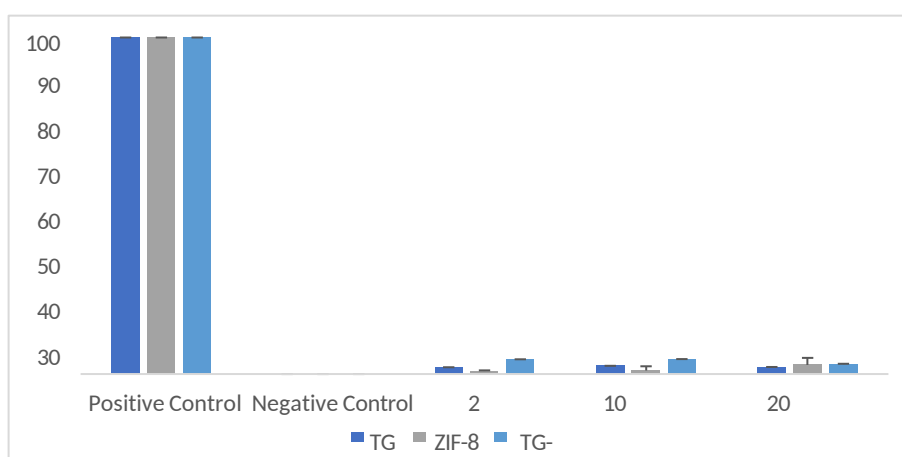


Figure 3.14. Hemolysis rates of 6-TG, ZIF-8 and 6-TG@ZIF-8 (5 mg/mL)

### 3.3.2.2. UiO-66 and 6-TG@UiO-66 Nanoparticles

2  $\mu\text{g/mL}$ , 10  $\mu\text{g/mL}$  and 20  $\mu\text{g/mL}$  as hemolysis rates of 6-TG, UiO-66 and 6-TG@UiO-66 nanoparticles were determined. The fact that these values are below 5% supports the biocompatibility of nanoparticles (Fig 3.15).

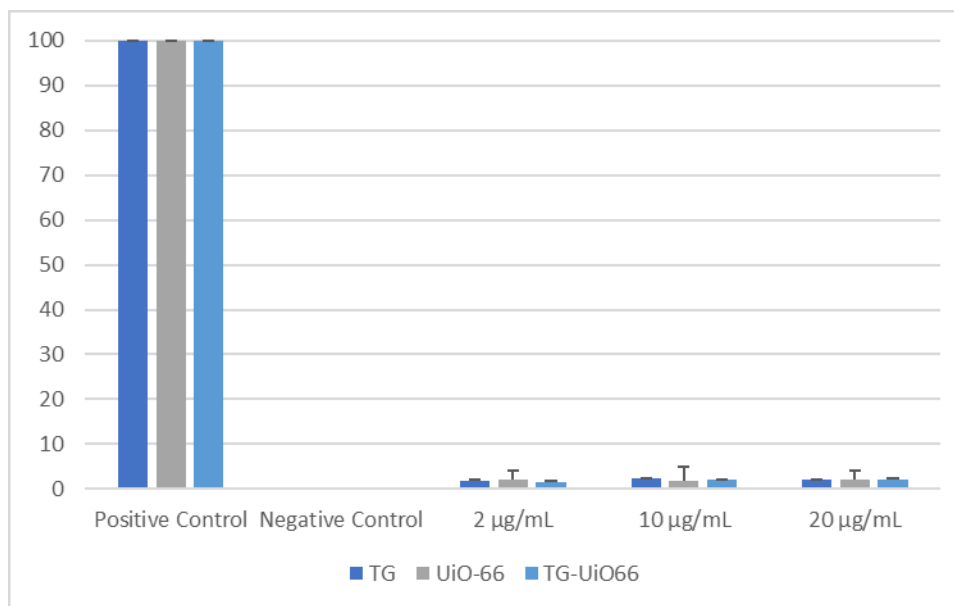


Figure 3.15. Hemolysis rates of 6-TG, UiO-66 and 6-TG@UiO-66 (5 mg/mL)

## 3.4. Drug Release

In order to observe the change in drug release from the synthesized nanoparticles over time, pH 5 solution mimicking the acidic cancer cell environment and PBS buffer solutions with normal cell pH 7.4 were created.

### 3.4.1. ZIF-8 and 6-TG@ZIF-8 Nanoparticles

ZIF-8 nanoparticles were incubated in these two different pH environments at 150 rpm for five days. To calculate the amount of drug released in a certain period of time, the absorbance values of the supernatants were measured with a UV-Vis spectrophotometer. The cumulative emission graph obtained at pH 5 and 7.4 is in Fig 3.16.

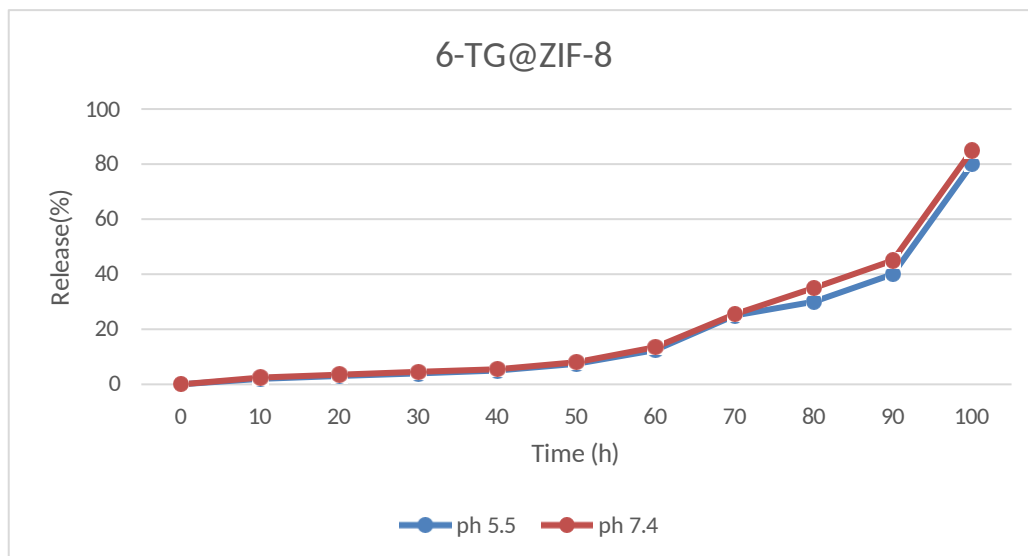


Figure 3.16. Drug release profiles of 6-TG, ZIF-8 and 6-TG@ZIF-8 (5 mg/mL)

### 3.4.2. UiO-66 and 6-TG@UiO-66 Nanoparticles

UiO-66 nanoparticles were incubated in these two different pH environments at 150 rpm for five days. To calculate the amount of drug released in a certain period of time, the absorbance values of the supernatants were measured with a UV-Vis spectrophotometer. The cumulative emission graph obtained at pH 5 and 7.4 is in Fig 3.17.

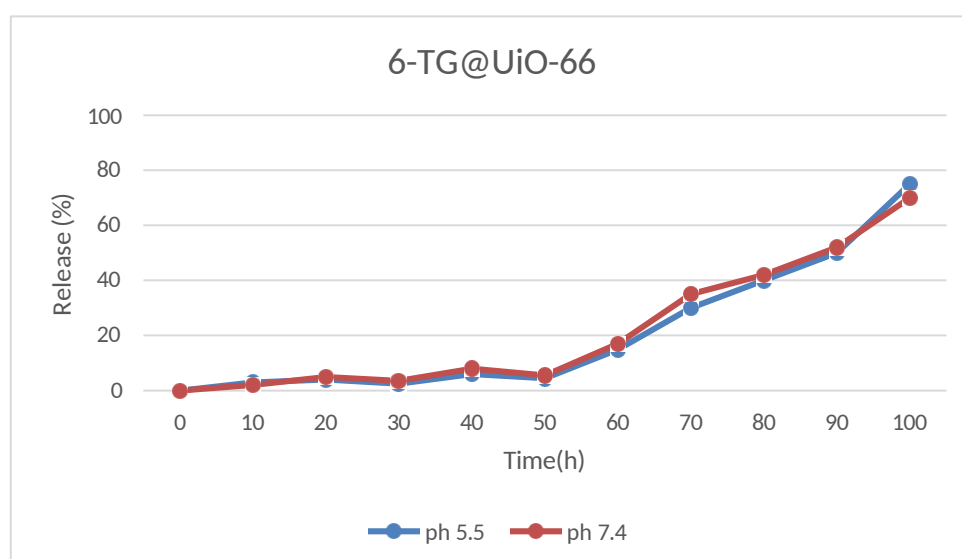


Figure 3.17. Drug release profiles of 6-TG, UiO-66 and 6-TG@UiO-66 (5 mg/mL)

### 3.5. Investigation of Antioxidant Activities

#### 3.5.1. ZIF-8 and 6-TG@ZIF-8 Nanoparticles

One popular technique for determining a compound's antioxidant potential is the DPPH assay. In solution, DPPH is a deep violet-colored, stable free radical. It gets reduced when it comes into contact with an antioxidant, which lowers the absorbance at 517 nm. The sample's antioxidant capability is directly correlated with the amount of color reduction. A sample with a higher proportion of inhibition has better antioxidant activity.

As can be seen from the graphs, the antioxidant capacity of 6-TG showed a gradual decrease in percentage depending on the concentration increase. ZIF-8 first showed a steady decrease and then an increase depending on the increase in concentration. As expected, the 6-TG@ZIF-8 nanoparticle we synthesized reached the highest percentage antioxidant capacity due to the increase in concentration, and thus our complex was much more successful than other substances in inhibiting oxidative stress.

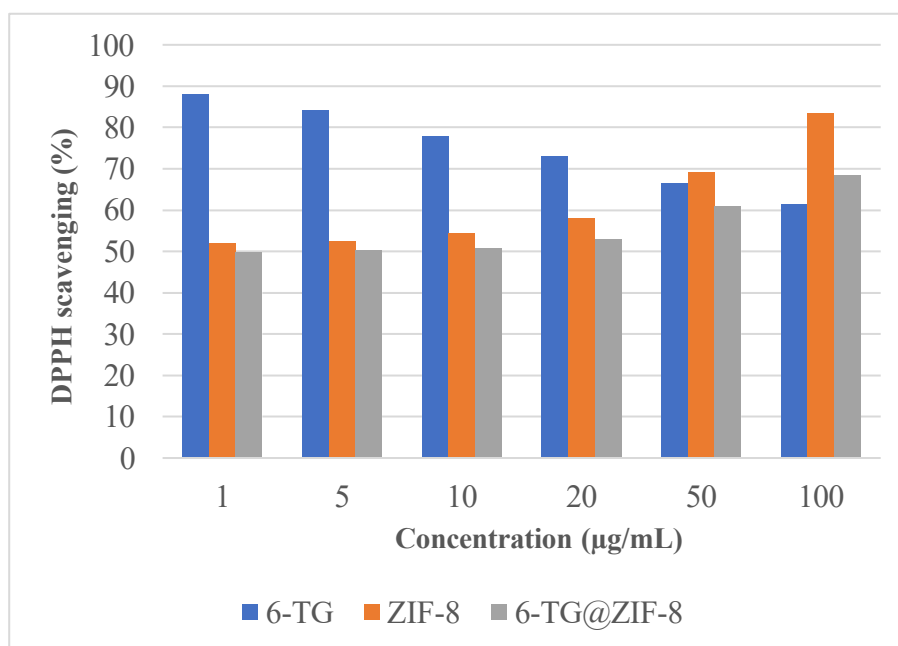


Figure 3.18. Antioxidant activities of 6-TG, ZIF-8 and 6-TG@ZIF-8 (5 mg/mL)

### 3.5.2. UiO-66 and 6-TG@UiO-66 Nanoparticles

As can be seen from the graphs, the antioxidant capacity of 6-TG showed a gradual decrease in percentage depending on the concentration increase. UiO-66 first showed a steady decrease, then showed an increase due to the increase in concentration. The 6-TG@UiO-66 nanoparticle we synthesized first decreased and then increased depending on the increase in concentration, reaching its maximum antioxidant capacity as a percentage.

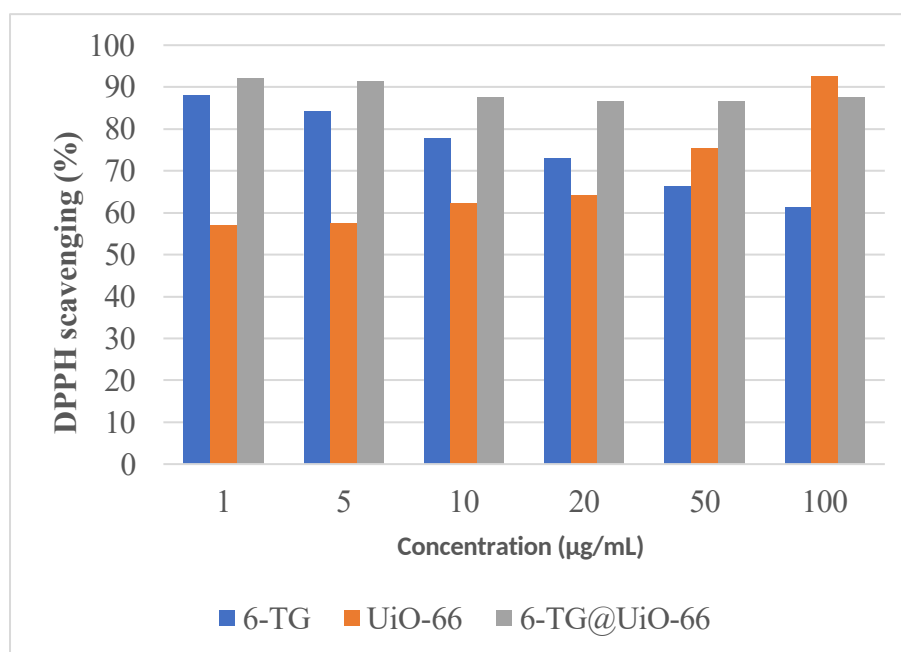


Figure 3.19. Antioxidant activities of 6-TG, UiO-66 and 6-TG@UiO-66 (5 mg/mL)

## 3.6. Investigation of Antibacterial Activities

### 3.6.1. ZIF-8 and 6-TG@ZIF-8 Nanoparticles

ZIF-8 MOF was tested on *S. Aureus* bacteria at 3,5,10 mg respectively, and as seen in the graphs, since an antibacterial effect was obtained at 5 and 10 mg, these concentrations were accepted as the MIC point. Likewise, these concentrations were also applied on *E. Coli* bacteria, respectively, and since we observed bacterial inhibition at most 10 mg, it was considered the MIC point. 6-TG was tested on *Staphylococcus Aureus* (*S. aureus*), a family of gram-positive bacteria, at 3,5,10 mg, respectively, and visible bacterial inhibition was detected at concentration of 10 mg. Therefore, 10 mg/ml was

considered the MIC point.

6-TG@ZIF-8 nanoparticle was tested at 3,5 and 10 mg on *S. aureus* bacteria and an antibacterial effect was observed and 10 mg/ml was chosen as the minimal inhibitory concentration (MIC) point. 6-TG was tested on *E. coli*, a family of gram-negative bacteria, at concentrations of 3,5 and 10 mg respectively, and a sufficient antibacterial effect was not observed. Since morphological deteriorations were observed in the bacterial colony formed when 40 mg was applied, a concentration above 40 mg was not tested.

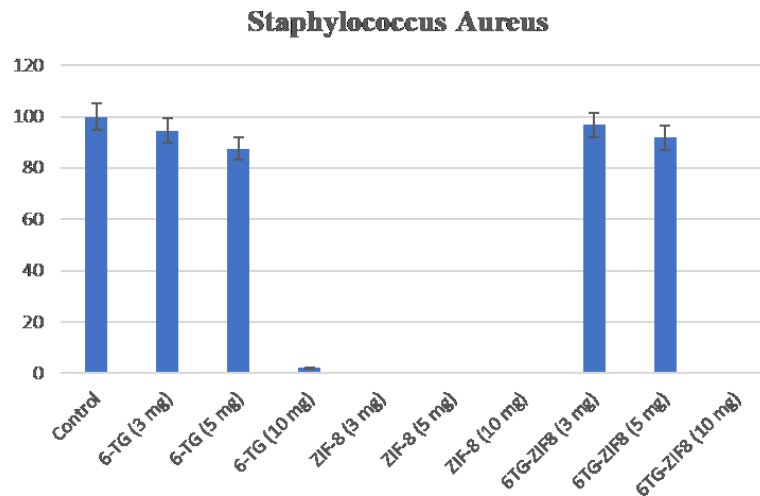


Figure 3.20. Antibacterial activities of 6-TG, ZIF-8 and 6-TG@ZIF-8

3,5 and 10 mg of 6-TG@ZIF-8 nanoparticle was tested in *E. coli* bacteria, and 10 mg/ml was chosen as the minimal inhibitory concentration (MIC) point because we observed a high number of bacterial inhibition.

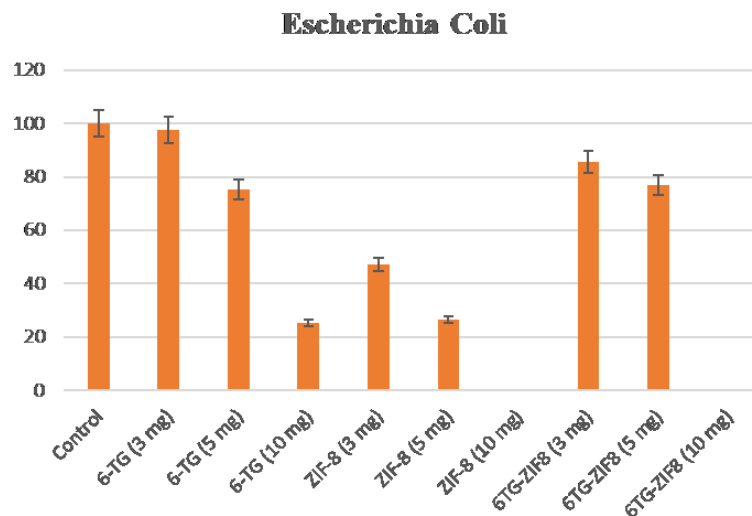


Figure 3.21. Antibacterial activities of 6-TG, ZIF-8 and 6-TG@ZIF-8

### 3.6.2. UiO-66 and 6-TG@UiO-66 Nanoparticles

UiO-66 MOF 3, 5 and 10 mg were tested on *S. aureus* bacteria, respectively, and as seen in the graphics, 10 mg was chosen as the MIC point since the antibacterial effect was seen at 10 mg and later. Likewise, these concentrations were also applied on *E. coli* bacteria, respectively, and since we observed bacterial inhibition at most at 10 mg, it was considered as the MIC point. 6-TG was tested on *Staphylococcus Aureus* (*S. aureus*), a family of gram-positive bacteria, at 3,5,10 mg, respectively, and visible bacterial inhibition was detected at 10 mg. Therefore, 10 mg/ml was accepted as the MIC point. 3,5 and 10 mg of 6-TG@UiO-66 nanoparticle was tested and since visible bacterial inhibition was detected in 10 mg, this concentration was accepted as the MIC point. 6-TG was tested on *E. coli*, a family of gram-negative bacteria, at concentrations of 3,5,10 mg, respectively, and a sufficient antibacterial effect was not observed. Since morphological deteriorations were observed in the bacterial colony formed when 40 mg was applied, a concentration above 40 mg was not tested. 3, 5 and 10 mg of 6-TG@UiO-66 nanoparticle were tested on *E. coli*, respectively, and no antibacterial effect was observed. Since morphological deteriorations occurred at 10 mg and later, no further trials were taken.

To summarize, while we detected an antibacterial effect at higher concentrations in UiO-66 MOF, we detected lower concentrations of MIC points in ZIF-8 compared to UiO-66. Likewise, in our drug-MOF complex, we found a MIC point at higher concentrations for the UiO-66 complex, while we found a MIC point at lower concentrations for the ZIF-8 complex. While the drug alone could not observe an antibacterial effect on gram negative bacteria, sufficient bacterial inhibition was observed at low concentrations on gram positive bacteria. The general conclusion to be drawn from this is that the drug-MOF complex has more bacterial properties than the drug or MOF alone and is effective on gram positive bacteria, especially at low concentration ranges. In short, our complex showed a greater antibacterial effect on gram-positive bacteria than gram-negative bacteria.

## Staphylococcus Aureus

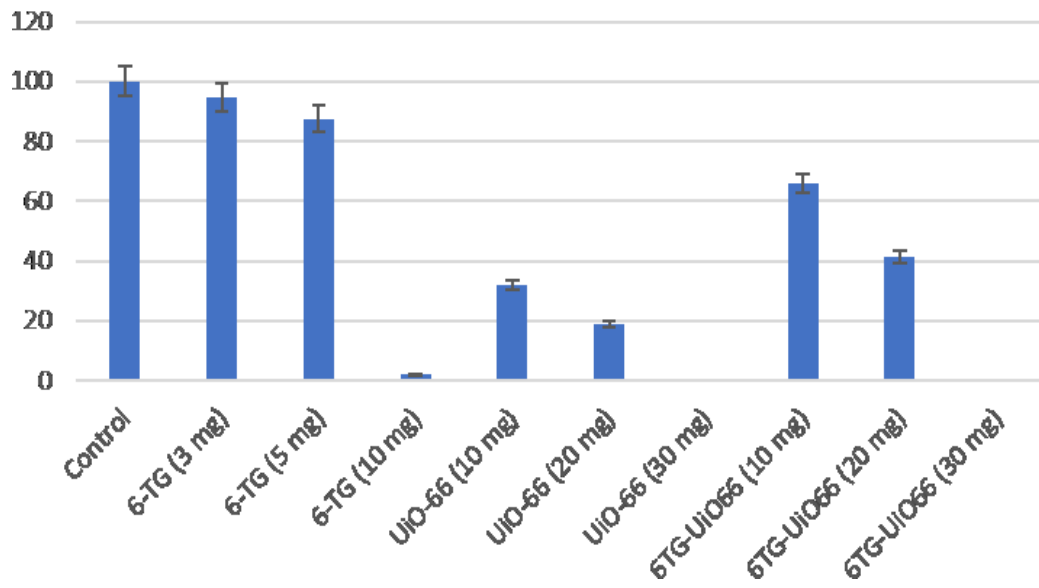


Figure 3.22. Antibacterial activities of 6-TG, UiO-66 and 6-TG@UiO-66

## Escherichia Coli

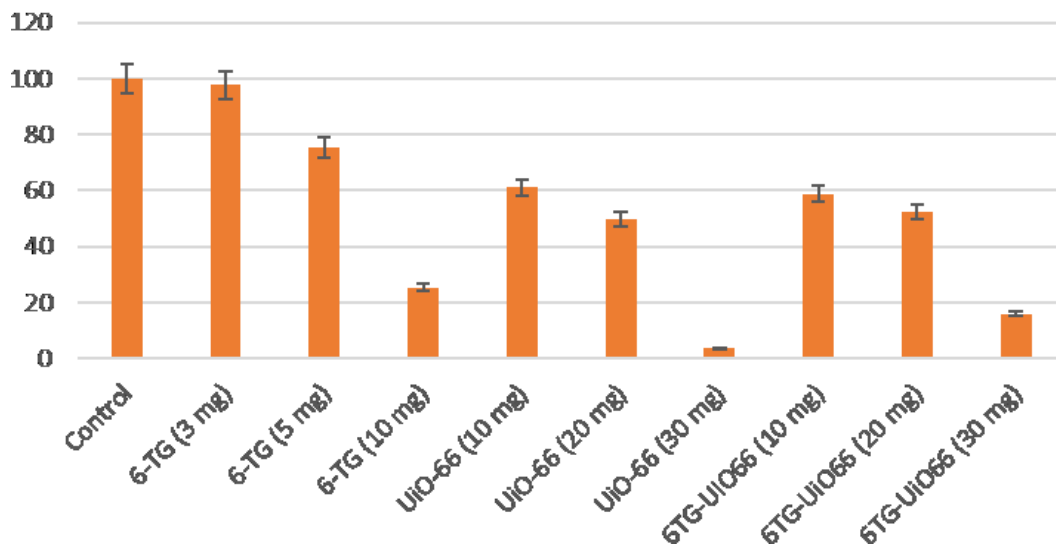


Figure 3.23. Antibacterial activities of 6-TG, UiO-66 and 6-TG@UiO-66

## CHAPTER 4

### CONCLUSION

In this thesis, we first synthesized ZIF-8 and UiO-66 metal organic frameworks and calculated their percentage efficiency. Then, by taking advantage of the literature, the calibration curve was drawn by taking the absorbance measurement of the 6-TG drug, and by encapsulating 6-TG into the metal organic frameworks we synthesized, we obtained 6-TG@ZIF-8 and 6-TG@UiO-66 and calculated the drug loading efficiencies in these nanoparticles. Then, SEM analysis was performed to observe the morphology and find the radius of the nanoparticles we synthesized, and we obtained the best results both morphologically and in radius at 5 mg/ml. In addition, EDX, FTIR, XRD, DLS, Zeta potential and TGA analyzes were performed and the characterization analyzes of the nanoparticles were completed. After the characterization analyzes, serum and hemolysis experiments were performed to check the biocompatibility of the nanoparticles. In addition, a drug release experiment was conducted to examine the drug release of the substances. In addition to all these, DPPH assay was carried out to examine the antioxidant activities of the substances and oxidative stress inhibition rates were calculated as a percentage, and antibacterial tests were carried out on *E. coli* and *S. aureus* bacteria by serial dilution method in order to observe the bacterial inhibition of the substances.

In conclusion, we hope that the properties exhibited by the 6-TG@ZIF-8 and 6-TG@UiO-66 we created may be a potential candidate in drug-MOF-based nanocomplexes.

## REFERENCES

- Skipper HE, Schabel FM, Wilcox WS. Experimental evaluation of potential anti-cancer agents. XIII On the criteria and kinetics associated with „curability“ of experimental leukaemia. *Cancer Chemotherapy Reports*, 1964; 35: 1–111.
- Mitra, S. *et al.* 2022 ‘Hormonal therapy for gynecological cancers: How far has science progressed toward clinical applications?’, *Cancers*, 14(3), p. 759. doi:10.3390/cancers14030759.
- Jemal, A. *et al.* 2011 ‘Global cancer statistics’, *CA: A Cancer Journal for Clinicians*, 61(2), pp. 69–90. doi:10.3322/caac.20107.
- Siegel, R.L. *et al.* 2021 ‘Cancer statistics, 2021’, *CA: A Cancer Journal for Clinicians*, 71(1), pp. 7–33. doi:10.3322/caac.21654.
- Tang, W. *et al.* 2017 ‘Tumor origin detection with tissue-specific MIRNA and DNA methylation markers’, *Bioinformatics*, 34(3), pp. 398–406. doi:10.1093/bioinformatics/btx622.
- Sharma, G. *et al.* 2010 ‘Various types and management of breast cancer: An overview’, *Journal of Advanced Pharmaceutical Technology & Research*, 1(2), p. 109. doi:10.4103/2231-4040.72251.
- Rahman, Md.M. *et al.* 2022 ‘Natural therapeutics and nutraceuticals for lung diseases: Traditional significance, phytochemistry, and pharmacology’, *Biomedicine & Pharmacotherapy*, 150, p. 113041. doi:10.1016/j.biopha.2022.113041.
- Islam, Md.R. *et al.* 2022 ‘Natural small molecules in breast cancer treatment: Understandings from a therapeutic viewpoint’, *Molecules*, 27(7), p. 2165. doi:10.3390/molecules27072165.
- Yan, J. *et al.* 2020 ‘Chiral protein supraparticles for tumor suppression and synergistic immunotherapy: An enabling strategy for bioactive supramolecular chirality construction’, *Nano Letters*, 20(8), pp. 5844–5852. doi:10.1021/acs.nanolett.0c01757.
- Yang, W. *et al.* 2023 ‘Turning chiral peptides into a racemic supraparticle to induce the self-degradation of MDM2’, *Journal of Advanced Research*, 45, pp. 59–71. doi:10.1016/j.jare.2022.05.009.
- Liu, C. *et al.* 2022 ‘Engineered extracellular vesicles and their mimetics for cancer immunotherapy’, *Journal of Controlled Release*, 349, pp. 679–698. doi:10.1016/j.jconrel.2022.05.062.

Sun, S. *et al.* 2023 ‘Selection and identification of a novel ssDNA aptamer targeting human skeletal muscle’, *Bioactive Materials*, 20, pp. 166–178. doi:10.1016/j.bioactmat.2022.05.016.

Hashemzahi, M. *et al.* 2018 ‘Phytosomal-curcumin antagonizes cell growth and migration, induced by thrombin through AMP-kinase in breast cancer’, *Journal of Cellular Biochemistry*, 119(7), pp. 5996–6007. doi:10.1002/jcb.26796.

Das, C.K. *et al.* 2018 ‘Bag3 overexpression and cytoprotective autophagy mediate apoptosis resistance in chemoresistant breast cancer cells’, *Neoplasia*, 20(3), pp. 263–279. doi:10.1016/j.neo.2018.01.001.

Ozols, R.F. *et al.* 2003 ‘Phase III trial of carboplatin and paclitaxel compared with Cisplatin and paclitaxel in patients with optimally resected stage III ovarian cancer: A Gynecologic Oncology Group Study’, *Journal of Clinical Oncology*, 21(17), pp. 3194–3200. doi:10.1200/jco.2003.02.153.

Drummond, A.J. and Waigh, R.D. 2000 *Recent Research Developments in Phytochemistry*.

Wiegand, I. *et al.* 2007 ‘Detection of extended-spectrum beta-lactamases among *enterobacteriaceae* by use of semiautomated microbiology systems and manual detection procedures’, *Journal of Clinical Microbiology*, 45(4), pp. 1167–1174. doi:10.1128/jcm.01988-06.

Kahlmeter, G. 2003 ‘European harmonization of MIC breakpoints for antimicrobial susceptibility testing of bacteria’, *Journal of Antimicrobial Chemotherapy*, 52(2), pp. 145–148. doi:10.1093/jac/dkg312.

Breijyeh, Z., Jubeh, B. and Karaman, R. 2020 ‘Resistance of gram-negative bacteria to current antibacterial agents and approaches to resolve it’, *Molecules*, 25(6), p. 1340. doi:10.3390/molecules25061340.

Mai-Prochnow, A. *et al.* 2016 ‘Gram positive and gram negative bacteria differ in their sensitivity to cold plasma’, *Scientific Reports*, 6(1). doi:10.1038/srep38610.

Pajerski, W. *et al.* 2019 ‘Attachment efficiency of gold nanoparticles by gram-positive and gram-negative bacterial strains governed by surface charges’, *Journal of Nanoparticle Research*, 21(8). doi:10.1007/s11051-019-4617-z.

Thairu, Y., Usman, Y. and Nasir, I. 2014 ‘Laboratory perspective of Gram staining and its significance in investigations of infectious diseases’, *Sub-Saharan African Journal of Medicine*, 1(4), p. 168. doi:10.4103/2384-5147.144725.

- Lambert, P.A. 2002 ‘Cellular impermeability and uptake of biocides and antibiotics in gram-positive bacteria and Mycobacteria’, *Journal of Applied Microbiology*, 92. doi:10.1046/j.1365-2672.92.5s1.7.x.
- Sannes, M.R. *et al.* 2004 ‘Virulence factor profiles and phylogenetic background of *Escherichia coli* isolates from veterans with bacteremia and uninfected control subjects’, *The Journal of Infectious Diseases*, 190(12), pp. 2121–2128. doi:10.1086/425984.
- Guiral, E. *et al.* 2010 ‘Prevalence of *Escherichia coli* among samples collected from the genital tract in pregnant and nonpregnant women: Relationship with virulence’, *FEMS Microbiology Letters*, 314(2), pp. 170–173. doi:10.1111/j.1574-6968.2010.02160.x.
- Levy, S.B. and Marshall, B. 2004 ‘Antibacterial resistance worldwide: Causes, challenges and responses’, *Nature Medicine*, 10(S12). doi:10.1038/nm1145.
- Lowy, F.D. 1998 ‘*Staphylococcus aureus* infections’, *New England Journal of Medicine*, 339(8), pp. 520–532. doi:10.1056/nejm199808203390806.
- Rasigade, J.-P. and Vandenesch, F. 2014 ‘*Staphylococcus aureus*: A pathogen with still unresolved issues’, *Infection, Genetics and Evolution*, 21, pp. 510–514. doi:10.1016/j.meegid.2013.08.018.
- Tong, S.Y. *et al.* 2015 ‘*Staphylococcus aureus* infections: Epidemiology, pathophysiology, clinical manifestations, and management’, *Clinical Microbiology Reviews*, 28(3), pp. 603–661. doi:10.1128/cmr.00134-14.
- Hill, D. *et al.* 2018 ‘The *Lactobacillus casei* group: History and health related applications’, *Frontiers in Microbiology*, 9. doi:10.3389/fmicb.2018.02107.
- Liguori, I. *et al.* 2018 ‘Oxidative stress, aging, and diseases’, *Clinical Interventions in Aging*, Volume 13, pp. 757–772. doi:10.2147/cia.s158513.
- Kurutas, E.B. 2016 ‘The importance of antioxidants which play the role in cellular response against oxidative/nitrosative stress: Current State’, *Nutrition Journal*, 15(1). doi:10.1186/s12937-016-0186-5.
- Feng, T. and Wang, J. 2020 ‘Oxidative stress tolerance and antioxidant capacity of lactic acid bacteria as probiotic: A systematic review’, *Gut Microbes*, 12(1), p. 1801944. doi:10.1080/19490976.2020.1801944.
- Wang, Yang *et al.* 2017 ‘Antioxidant properties of probiotic bacteria’, *Nutrients*, 9(5), p. 521. doi:10.3390/nu9050521.
- Chistyakov, V. *et al.* 2018 ‘The use of biosensors to explore the potential of probiotic strains to reduce the SOS response and mutagenesis in bacteria’, *Biosensors*, 8(1), p. 25. doi:10.3390/bios8010025.

Munteanu, I.G. and Apetrei, C. 2021 'Analytical methods used in determining antioxidant activity: A Review', *International Journal of Molecular Sciences*, 22(7), p. 3380. doi:10.3390/ijms22073380.

Prieto, M.A., Vázquez, J.A. and Murado, M.A. 2015 'Crocin bleaching antioxidant assay revisited: Application to microplate to analyse antioxidant and pro-oxidant activities', *Food Chemistry*, 167, pp. 299–310. doi:10.1016/j.foodchem.2014.06.114.

Adcock, J.L. *et al.* 2014 'Advances in the use of acidic potassium permanganate as a chemiluminescence reagent: A Review', *Analytica Chimica Acta*, 807, pp. 9– 28. doi:10.1016/j.aca.2013.11.016.

Zampini, I.C., Ordoñez, R.M. and Isla, M.I. 2010 'Autographic assay for the rapid detection of antioxidant capacity of liquid and semi-solid pharmaceutical formulations using ABTS+ immobilized by gel entrapment', *AAPS PharmSciTech*, 11(3), pp. 1159–1163. doi:10.1208/s12249-010-9484-y.

Cacig, S., Szabo-Raluca, M. and Lupea, A. 2006 'Spectrophotometric method for the study of the antioxidant activity applied on Ziziphus jujuba and Hydrangea paniculata aqueous extract', *Zbornik Matice srpske za prirodne nauke*, (111), pp. 87–93. doi:10.2298/zmspn0611087c.

Kasote, D.M., Jayaprakasha, G.K. and Patil, B.S. 2019 'Leaf disc assays for rapid measurement of antioxidant activity', *Scientific Reports*, 9(1). doi:10.1038/s41598-018-38036-x.

Popović, B.M. *et al.* 2012 'Antioxidant capacity of Cornelian Cherry (Cornus Mas L.) – comparison between permanganate reducing antioxidant capacity and other antioxidant methods', *Food Chemistry*, 134(2), pp. 734–741. doi:10.1016/j.foodchem.2012.02.170.

Zhou, Y., Zhang, M. and Liu, H. 2015 'Total antioxidant capacity of serum determined using the potassium permanganate agar method based on serum diffusion in agar', *Bioinorganic Chemistry and Applications*, 2015, pp. 1–6. doi:10.1155/2015/406071.

Pyrzynska, K. and Pękal, A. 2013 'Application of free radical diphenylpicrylhydrazyl (DPPH) to estimate the antioxidant capacity of food samples', *Analytical Methods*, 5(17), p. 4288. doi:10.1039/c3ay40367j.

Schaich, K.M., Tian, X. and Xie, J. 2015 'Hurdles and pitfalls in measuring antioxidant efficacy: A critical evaluation of ABTS, DPPH, and Orac assays', *Journal of Functional Foods*, 14, pp. 111–125. doi:10.1016/j.jff.2015.01.043.

Staško, A. *et al.* 2007 'The potential pitfalls of using 1,1-diphenyl-2- picrylhydrazyl to characterize antioxidants in mixed water solvents', *Free Radical Research*, 41(4), pp. 379–390. doi:10.1080/10715760600930014.

Miller, N.J. *et al.* 1993 'A novel method for measuring antioxidant capacity and its application to monitoring the antioxidant status in premature neonates', *Clinical Science*, 84(4), pp. 407–412. doi:10.1042/cs0840407.

Ilyasov, I.R. *et al.* 2020 'ABTS/pp decolorization assay of antioxidant capacity reaction pathways', *International Journal of Molecular Sciences*, 21(3), p. 1131. doi:10.3390/ijms21031131.

Ivekovic, D. *et al.* 2005 'Evaluation of the antioxidant activity by flow injection analysis method with electrochemically generated ABTS radical cation', *The Analyst*, 130(5), p. 708. doi:10.1039/b415939j.

Tian, X. and Schaich, K.M. 2013 'Effects of molecular structure on kinetics and dynamics of the trolox equivalent antioxidant capacity assay with abts+', *Journal of Agricultural and Food Chemistry*, 61(23), pp. 5511–5519. doi:10.1021/jf4010725.

Karran, P. and Attard, N. 2008 'Thiopurines in current medical practice: Molecular mechanisms and contributions to therapy-related cancer', *Nature Reviews Cancer*, 8(1), pp. 24–36. doi:10.1038/nrc2292.

Munshi, P.N., Lubin, M. and Bertino, J.R. 2014 '6-thioguanine: A drug with unrealized potential for cancer therapy', *The Oncologist*, 19(7), pp. 760–765. doi:10.1634/theoncologist.2014-0178.

Issaeva, N. *et al.* 2010 '6-thioguanine selectively kills BRCA2-defective tumors and overcomes PARP inhibitor resistance', *Cancer Research*, 70(15), pp. 6268– 6276. doi:10.1158/0008-5472.can-09-3416.

Evans, W.E. 2004 'Pharmacogenetics of thiopurine S-methyltransferase and thiopurine therapy', *Therapeutic Drug Monitoring*, 26(2), pp. 186–191. doi:10.1097/00007691-200404000-00018.

de Boer, N.K. *et al.* 2007 'Drug insight: Pharmacology and toxicity of thiopurine therapy in patients with IBD', *Nature Clinical Practice Gastroenterology & Hepatology*, 4(12), pp. 686–694. doi:10.1038/ncpgasthep1000.

Yamane, K., Schupp, J.E. and Kinsella, T.J. 2007 'BRCA1 activates a G2-M cell cycle checkpoint following 6-thioguanine-induced DNA mismatch damage', *Cancer Research*, 67(13), pp. 6286–6292. doi:10.1158/0008-5472.can-06-2205.

Warren, D.J., Anderson, A. and Slordal, L. 1995 *Quantitation of 6-thioguanine residues in peripheral blood leukocyte DNA obtained from patients receiving 6-mercaptopurine-based maintenance therapy.*

Abánades Lázaro, I., Wells, C.J. and Forgan, R.S. 2020 'Multivariate modulation of the zirconium-based MOF-66 for defect-controlled Combination Anticancer Drug Delivery', *Angewandte Chemie*, 132(13), pp. 5249–5255. doi:10.1002/ange.201915848.

- Ma, M. 2011 *Preparation, characterization of metal-organic frameworks for biological applications*.
- Wu, H., Zhou, W. and Yildirim, T. 2009 'High-capacity methane storage in metal-organic frameworks M2(dhtp): The important role of open metal sites', *Journal of the American Chemical Society*, 131(13), pp. 4995–5000. doi:10.1021/ja900258t.
- Zacher, D. *et al.* 2009 'Thin films of metal-organic frameworks', *Chemical Society Reviews*, 38(5), p. 1418. doi:10.1039/b805038b.
- Platero Prats, A.E. *et al.* 2010 'Heterogeneous catalysis with alkaline-earth metal-based mofs: A green calcium catalyst', *ChemCatChem*, 2(2), pp. 147–149. doi:10.1002/cctc.200900228.
- Platero-Prats, A.E. *et al.* 2011 'From coordinatively weak ability of constituents to very stable alkaline-earth sulfonate metal-organic frameworks', *Crystal Growth & Design*, 11(5), pp. 1750–1758. doi:10.1021/cg200078j.
- Yang, L.-M. *et al.* 2011 'Revisiting isoreticular mofs of Alkaline Earth Metals: A comprehensive study on phase stability, electronic structure, chemical bonding, and optical properties of A-IRMOF-1 (A = be, Mg, Ca, sr, BA)', *Physical Chemistry Chemical Physics*, 13(21), p. 10191. doi:10.1039/c0cp02944k.
- Reineke, T.M. *et al.* 1999 'A microporous lanthanide-organic framework', *Angewandte Chemie International Edition*, 38(17), pp. 2590–2594. doi:10.1002/(sici)1521-3773(19990903)38:17<2590::aid-anie2590>3.0.co;2-h.
- Serpaggi, F. and Férey, G. 1998 'Hybrid open frameworks (MIL-N). part 4 synthesis and crystal structure of MIL-8, a series of lanthanide glutarates with an open framework, [Ln(h<sub>2</sub>o)]<sub>2</sub>[o<sub>2</sub>c(ch<sub>2</sub>)<sub>3</sub>co<sub>2</sub>]<sub>3</sub>·4h<sub>2</sub>o', *Journal of Materials Chemistry*, 8(12), pp. 2737–2741. doi:10.1039/a802713g.
- Serre, C. *et al.* 2002 'Hydrothermal synthesis, structure determination, and thermal behavior of new three-dimensional europium terephthalates: MIL-511t,ht and MIL-52 or EU2n(oh)<sub>x</sub>(h<sub>2</sub>o)<sub>y</sub>(o<sub>2</sub>C-C<sub>6</sub>H<sub>4</sub>-co<sub>2</sub>)<sub>z</sub> (n = III, III, II; x = 4, 0, 0; y = 2, 0, 0; z = 1, 1, 2)', *Chemistry of Materials*, 14(5), pp. 2409–2415. doi:10.1021/cm0211148.
- Serre, C. and Férey, G. 2002 'Hydrothermal synthesis, thermal behaviour and structure determination from powder data of a porous three-dimensional europium trimesate: EU3(h<sub>2</sub>o)(oh)<sub>6</sub>[c<sub>6</sub>H<sub>3</sub>(co<sub>2</sub>)<sub>3</sub>]·3h<sub>2</sub>O or MIL-63', *J. Mater. Chem.*, 12(10), pp. 3053–3057. doi:10.1039/b203763g.
- Yaghi, O.M. *et al.* 2003 'Reticular synthesis and the design of new materials', *Nature*, 423(6941), pp. 705–714. doi:10.1038/nature01650.

Sumida, K., Rogow, D. and Mason, J. 2012 ‘Carbon dioxide capture in metal-organic frameworks’, *Chemical Reviews*.

Wang, C.-C. and Ying, J.Y. 1999 ‘Sol–gel synthesis and hydrothermal processing of anatase and Rutile Titania Nanocrystals’, *Chemistry of Materials*, 11(11), pp. 3113–3120. doi:10.1021/cm990180f.

Cravillon, J. *et al.* 2009 ‘Rapid room-temperature synthesis and characterization of nanocrystals of a prototypical zeolitic imidazolate framework’, *Chemistry of Materials*, 21(8), pp. 1410–1412. doi:10.1021/cm900166h.

Huang, L., Wang, H. and Chen, J. 2003 ‘Synthesis, morphology control, and properties of porous metal–organic coordination polymers’, *Microporous and Mesoporous Materials*, 58(2), pp. 105–114. doi:10.1016/s1387-1811(02)00609-1.

Tranchemontagne, D.J., Hunt, J.R. and Yaghi, O.M. 2008 ‘Room temperature synthesis of metal-organic frameworks: MOF-5, MOF-74, MOF-177, MOF-199, and IRMOF-0’, *Tetrahedron*, 64(36), pp. 8553–8557. doi:10.1016/j.tet.2008.06.036.

Biemmi, E. *et al.* 2009 ‘High-throughput screening of synthesis parameters in the formation of the metal-organic frameworks MOF-5 and HKUST-1’, *Microporous and Mesoporous Materials*, 117(1–2), pp. 111–117. doi:10.1016/j.micromeso.2008.06.040.

Nouar, F. *et al.* 2009 ‘Zeolite-like metal–organic frameworks (zmofs) as hydrogen storage platform: Lithium and magnesium ion-exchange and H<sub>2</sub>- (Rho- ZMOF) Interaction Studies’, *Journal of the American Chemical Society*, 131(8), pp. 2864–2870. doi:10.1021/ja807229a.

Braga, D. *et al.* 2007 ‘Solvent effect in a “Solvent free” reaction’, *CrystEngComm*, 9(10), p. 879. doi:10.1039/b711983f.

Pichon, A. and James, S.L. 2008 ‘An array-based study of reactivity under solvent-free mechanochemical conditions—insights and Trends’, *CrystEngComm*, 10(12), p. 1839. doi:10.1039/b810857a.

Stock, N. and Biswas, S. 2011 ‘Synthesis of metal-organic frameworks (mofs): Routes to various MOF topologies, morphologies, and composites’, *Chemical Reviews*, 112(2), pp. 933–969. doi:10.1021/cr200304e.

Pichon, A., Lazuen-Garay, A. and James, S.L. 2006 ‘Solvent-free synthesis of a microporous metal–organic framework’, *CrystEngComm*, 8(3), p. 211. doi:10.1039/b513750k.

- Shinde, D.B. *et al.* 2016 'A mechanochemically synthesized covalent organic framework as a proton-conducting solid electrolyte', *Journal of Materials Chemistry A*, 4(7), pp. 2682–2690. doi:10.1039/c5ta10521h.
- Friščić, T. and Fábián, L. 2009 'Mechanochemical conversion of a metal oxide into coordination polymers and porous frameworks using liquid-assisted grinding (LAG)', *CrystEngComm*, 11(5), p. 743. doi:10.1039/b822934c.
- Gedanken, A. 2004 'Sonochemical synthesis of amorphous iron', *Ultrason Sonochem*, 11(47).
- Suslick, K.S. *et al.* 1991 'Sonochemical synthesis of amorphous iron', *Nature*, 353(6343), pp. 414–416. doi:10.1038/353414a0.
- Sono, T., Mingos, D. and Baghurst, D. 2004 'Novel energy source for reactions. In: The new chemistry.', *Cambridge:Syndicate of the University of Cambridge*. Edited by N. Hall.
- Qiu, L.-G. *et al.* 2008 'Facile synthesis of nanocrystals of a microporous metal–organic framework by an ultrasonic method and selective sensing of organoamines', *Chemical Communications*, (31), p. 3642. doi:10.1039/b804126a.
- Li, Z.-Q. *et al.* 2009 'Ultrasonic synthesis of the microporous metal–organic framework CU<sub>3</sub>(BTC)<sub>2</sub> at ambient temperature and pressure: An efficient and environmentally friendly method', *Materials Letters*, 63(1), pp. 78–80. doi:10.1016/j.matlet.2008.09.010.
- Lee, D.-E. *et al.* 2012 'Multifunctional nanoparticles for multimodal imaging and theragnosis', *Chem. Soc. Rev.*, 41(7), pp. 2656–2672. doi:10.1039/c2cs15261d.
- Cai, W. *et al.* 2018 'Metal–organic framework-based stimuli-responsive systems for Drug Delivery', *Advanced Science*, 6(1). doi:10.1002/advs.201801526.
- Lu, K. *et al.* 2018 'Nanoscale Metal–organic frameworks for therapeutic, imaging, and sensing applications', *Advanced Materials*, 30(37). doi:10.1002/adma.201707634.
- Liguori, I. *et al.* 2018 'Oxidative stress, aging, and diseases', *Clinical Interventions in Aging*, Volume 13, pp. 757–772. doi:10.2147/cia.s158513.
- Kurutas, E.B. 2016 'The importance of antioxidants which play the role in cellular response against oxidative/nitrosative stress: Current State', *Nutrition Journal*, 15(1). doi:10.1186/s12937-016-0186-5.
- Feng, T. and Wang, J. 2020 'Oxidative stress tolerance and antioxidant capacity of lactic acid bacteria as probiotic: A systematic review', *Gut Microbes*, 12(1), p. 1801944. doi:10.1080/19490976.2020.1801944.

Wang, Yang *et al.* 2017 ‘Antioxidant properties of probiotic bacteria’, *Nutrients*, 9(5), p. 521. doi:10.3390/nu9050521.

Chistyakov, V. *et al.* 2018 ‘The use of biosensors to explore the potential of probiotic strains to reduce the SOS response and mutagenesis in bacteria’, *Biosensors*, 8(1), p. 25. doi:10.3390/bios8010025.

Munteanu, I.G. and Apetrei, C. 2021 ‘Analytical methods used in determining antioxidant activity: A Review’, *International Journal of Molecular Sciences*, 22(7), p. 3380. doi:10.3390/ijms22073380.

Prieto, M.A., Vázquez, J.A. and Murado, M.A. 2015 ‘Crocic acid bleaching antioxidant assay revisited: Application to microplate to analyse antioxidant and pro-oxidant activities’, *Food Chemistry*, 167, pp. 299–310. doi:10.1016/j.foodchem.2014.06.114.

Adcock, J.L. *et al.* 2014 ‘Advances in the use of acidic potassium permanganate as a chemiluminescence reagent: A Review’, *Analytica Chimica Acta*, 807, pp. 9– 28. doi:10.1016/j.aca.2013.11.016.

Zampini, I.C., Ordoñez, R.M. and Isla, M.I. 2010 ‘Autographic assay for the rapid detection of antioxidant capacity of liquid and semi-solid pharmaceutical formulations using ABTS+ immobilized by gel entrapment’, *AAPS PharmSciTech*, 11(3), pp. 1159–1163. doi:10.1208/s12249-010-9484-y.

Cacig, S., Szabo-Raluca, M. and Lupea, A. 2006 ‘Spectrophotometric method for the study of the antioxidant activity applied on *Ziziphus jujuba* and *Hydrangea paniculata* aqueous extract’, *Zbornik Matice srpske za prirodne nauke*, (111), pp. 87–93. doi:10.2298/zmspn0611087c.

Kasote, D.M., Jayaprakasha, G.K. and Patil, B.S. 2019 ‘Leaf disc assays for rapid measurement of antioxidant activity’, *Scientific Reports*, 9(1). doi:10.1038/s41598-018-38036-x.

Popović, B.M. *et al.* 2012 ‘Antioxidant capacity of Cornelian Cherry (*Cornus Mas* L.) – comparison between permanganate reducing antioxidant capacity and other antioxidant methods’, *Food Chemistry*, 134(2), pp. 734–741. doi:10.1016/j.foodchem.2012.02.170.

Zhou, Y., Zhang, M. and Liu, H. 2015 ‘Total antioxidant capacity of serum determined using the potassium permanganate agar method based on serum diffusion in agar’, *Bioinorganic Chemistry and Applications*, 2015, pp. 1–6. doi:10.1155/2015/406071.

Pyrzyska, K. and Pękal, A. 2013 ‘Application of free radical diphenylpicrylhydrazyl (DPPH) to estimate the antioxidant capacity of food samples’, *Analytical Methods*, 5(17), p. 4288. doi:10.1039/c3ay40367j.

- Schaich, K.M., Tian, X. and Xie, J. 2015 'Hurdles and pitfalls in measuring antioxidant efficacy: A critical evaluation of ABTS, DPPH, and Orac assays', *Journal of Functional Foods*, 14, pp. 111–125. doi:10.1016/j.jff.2015.01.043.
- Staško, A. *et al.* 2007 'The potential pitfalls of using 1,1-diphenyl-2-picrylhydrazyl to characterize antioxidants in mixed water solvents', *Free Radical Research*, 41(4), pp. 379–390. doi:10.1080/10715760600930014.
- Miller, N.J. *et al.* 1993 'A novel method for measuring antioxidant capacity and its application to monitoring the antioxidant status in premature neonates', *Clinical Science*, 84(4), pp. 407–412. doi:10.1042/cs0840407.
- Ilyasov, I.R. *et al.* 2020 'ABTS/pp decolorization assay of antioxidant capacity reaction pathways', *International Journal of Molecular Sciences*, 21(3), p. 1131. doi:10.3390/ijms21031131.
- Ivekovic, D. *et al.* 2005 'Evaluation of the antioxidant activity by flow injection analysis method with electrochemically generated ABTS radical cation', *The Analyst*, 130(5), p. 708. doi:10.1039/b415939j.
- Tian, X. and Schaich, K.M. 2013 'Effects of molecular structure on kinetics and dynamics of the trolox equivalent antioxidant capacity assay with abts+', *Journal of Agricultural and Food Chemistry*, 61(23), pp. 5511–5519. doi:10.1021/jf4010725.
- Karran, P. and Attard, N. 2008 'Thiopurines in current medical practice: Molecular mechanisms and contributions to therapy-related cancer', *Nature Reviews Cancer*, 8(1), pp. 24–36. doi:10.1038/nrc2292.
- Munshi, P.N., Lubin, M. and Bertino, J.R. 2014 '6-thioguanine: A drug with unrealized potential for cancer therapy', *The Oncologist*, 19(7), pp. 760–765. doi:10.1634/theoncologist.2014-0178.
- Issaeva, N. *et al.* 2010 '6-thioguanine selectively kills BRCA2-defective tumors and overcomes PARP inhibitor resistance', *Cancer Research*, 70(15), pp. 6268–6276. doi:10.1158/0008-5472.can-09-3416.
- Evans, W.E. 2004 'Pharmacogenetics of thiopurine S-methyltransferase and thiopurine therapy', *Therapeutic Drug Monitoring*, 26(2), pp. 186–191. doi:10.1097/00007691-200404000-00018.
- de Boer, N.K. *et al.* 2007 'Drug insight: Pharmacology and toxicity of thiopurine therapy in patients with IBD', *Nature Clinical Practice Gastroenterology & Hepatology*, 4(12), pp. 686–694. doi:10.1038/ncpgasthep1000.
- Yamane, K., Schupp, J.E. and Kinsella, T.J. 2007 'BRCA1 activates a G2-M cell cycle checkpoint following 6-thioguanine-induced DNA mismatch damage', *Cancer Research*, 67(13), pp. 6286–6292. doi:10.1158/0008-5472.can-06-2205.

Warren, D.J., Anderson, A. and Slordal, L. 1995 *Quantitation of 6- thioguanine residues in peripheral blood leukocyte DNA obtained from patients receiving 6- mercaptopurine-based maintenance therapy.*

Abánades Lázaro, I., Wells, C.J. and Forgan, R.S. 2020 ‘Multivariate modulation of the zr mof uiio-66 for defect-controlled Combination Anticancer Drug Delivery’, *Angewandte Chemie*, 132(13), pp. 5249–5255. doi:10.1002/ange.201915848.

Ma, M. 2011 *Preparation, characterization of metal-organic frameworks for biological applications.*

Wu, H., Zhou, W. and Yildirim, T. 2009 ‘High-capacity methane storage in metal–organic frameworks M2(dhtp): The important role of open metal sites’, *Journal of the American Chemical Society*, 131(13), pp. 4995–5000. doi:10.1021/ja900258t.

Zacher, D. *et al.* 2009 ‘Thin films of metal–organic frameworks’, *Chemical Society Reviews*, 38(5), p. 1418. doi:10.1039/b805038b.

Platero Prats, A.E. *et al.* 2010 ‘Heterogeneous catalysis with alkaline-earth metal- based mofs: A green calcium catalyst’, *ChemCatChem*, 2(2), pp. 147–149. doi:10.1002/cctc.200900228.

Platero-Prats, A.E. *et al.* 2011 ‘From coordinatively weak ability of constituents to very stable alkaline-earth sulfonate metal–organic frameworks’, *Crystal Growth & Design*, 11(5), pp. 1750–1758. doi:10.1021/cg200078j.

Yang, L.-M. *et al.* 2011 ‘Revisiting isoreticular mofs of Alkaline Earth Metals: A comprehensive study on phase stability, electronic structure, chemical bonding, and optical properties of A–IRMOF-1 (A = be, Mg, Ca, sr, BA)’, *Physical Chemistry Chemical Physics*, 13(21), p. 10191. doi:10.1039/c0cp02944k.

Reineke, T.M. *et al.* 1999 ‘A microporous lanthanide-organic framework’, *Angewandte Chemie International Edition*, 38(17), pp. 2590–2594. doi:10.1002/(sici)1521-3773(19990903)38:17<2590::aid-anie2590>3.0.co;2-h.

Serpaggi, F. and Férey, G. 1998 ‘Hybrid open frameworks (MIL-N). part 4 synthesis and crystal structure of MIL-8, a series of lanthanide glutarates with an open framework, [Ln(h<sub>2</sub>o)]<sub>2</sub>[o<sub>2</sub>c(ch<sub>2</sub>)<sub>3</sub>co<sub>2</sub>]<sub>3</sub>·4h<sub>2</sub>o’, *Journal of Materials Chemistry*, 8(12), pp. 2737–2741. doi:10.1039/a802713g.

Serre, C. *et al.* 2002 ‘Hydrothermal synthesis, structure determination, and thermal behavior of new three-dimensional europium terephthalates: MIL- 511t,ht and MIL-52 or EU<sub>2n</sub>(oh)<sub>x</sub>(h<sub>2</sub>o)<sub>y</sub>(o<sub>2</sub>C–C<sub>6</sub>H<sub>4</sub>–co<sub>2</sub>)<sub>z</sub> (n = III, III, II; x = 4, 0, 0; y = 2, 0, 0; z = 1, 1, 2)’, *Chemistry of Materials*, 14(5), pp. 2409–2415. doi:10.1021/cm0211148.

- Serre, C. and Férey, G. 2002 'Hydrothermal synthesis, thermal behaviour and structure determination from powder data of a porous three-dimensional europium trimesate:  $\text{EU}_3(\text{h}_2\text{o})(\text{oh})_6[\text{c}_6\text{H}_3(\text{co}_2)_3] \cdot 3\text{h}_2\text{O}$  or MIL-63', *J. Mater. Chem.*, 12(10), pp. 3053–3057. doi:10.1039/b203763g.
- Yaghi, O.M. *et al.* 2003 'Reticular synthesis and the design of new materials', *Nature*, 423(6941), pp. 705–714. doi:10.1038/nature01650.
- Sumida, K., Rogow, D. and Mason, J. 2012 'Carbon dioxide capture in metal-organic frameworks', *Chemical Reviews*.
- Wang, C.-C. and Ying, J.Y. 1999 'Sol-gel synthesis and hydrothermal processing of anatase and Rutile Titania Nanocrystals', *Chemistry of Materials*, 11(11), pp. 3113–3120. doi:10.1021/cm990180f.
- Cravillon, J. *et al.* 2009 'Rapid room-temperature synthesis and characterization of nanocrystals of a prototypical zeolitic imidazolate framework', *Chemistry of Materials*, 21(8), pp. 1410–1412. doi:10.1021/cm900166h.
- Huang, L., Wang, H. and Chen, J. 2003 'Synthesis, morphology control, and properties of porous metal-organic coordination polymers', *Microporous and Mesoporous Materials*, 58(2), pp. 105–114. doi:10.1016/s1387-1811(02)00609-1.
- Tranchemontagne, D.J., Hunt, J.R. and Yaghi, O.M. 2008 'Room temperature synthesis of metal-organic frameworks: MOF-5, MOF-74, MOF-177, MOF-199, and IRMOF-0', *Tetrahedron*, 64(36), pp. 8553–8557. doi:10.1016/j.tet.2008.06.036.
- Biemmi, E. *et al.* 2009 'High-throughput screening of synthesis parameters in the formation of the metal-organic frameworks MOF-5 and HKUST-1', *Microporous and Mesoporous Materials*, 117(1–2), pp. 111–117. doi:10.1016/j.micromeso.2008.06.040.
- Nouar, F. *et al.* 2009 'Zeolite-like metal-organic frameworks (zmofs) as hydrogen storage platform: Lithium and magnesium ion-exchange and H<sub>2</sub>- (Rho- ZMOF) Interaction Studies', *Journal of the American Chemical Society*, 131(8), pp. 2864–2870. doi:10.1021/ja807229a.
- Braga, D. *et al.* 2007 'Solvent effect in a "Solvent free" reaction', *CrystEngComm*, 9(10), p. 879. doi:10.1039/b711983f.
- Pichon, A. and James, S.L. 2008 'An array-based study of reactivity under solvent-free mechanochemical conditions—insights and Trends', *CrystEngComm*, 10(12), p. 1839. doi:10.1039/b810857a.
- Stock, N. and Biswas, S. 2011 'Synthesis of metal-organic frameworks (mofs): Routes to various MOF topologies, morphologies, and composites', *Chemical Reviews*, 112(2), pp. 933–969. doi:10.1021/cr200304e.

- Pichon, A., Lazuen-Garay, A. and James, S.L. 2006 'Solvent-free synthesis of a microporous metal-organic framework', *CrystEngComm*, 8(3), p. 211. doi:10.1039/b513750k.
- Shinde, D.B. *et al.* 2016 'A mechanochemically synthesized covalent organic framework as a proton-conducting solid electrolyte', *Journal of Materials Chemistry A*, 4(7), pp. 2682–2690. doi:10.1039/c5ta10521h.
- Friščić, T. and Fábián, L. 2009 'Mechanochemical conversion of a metal oxide into coordination polymers and porous frameworks using liquid-assisted grinding (LAG)', *CrystEngComm*, 11(5), p. 743. doi:10.1039/b822934c.
- Gedanken, A. 2004 'Sonochemical synthesis of amorphous iron', *Ultrason Sonochem*, 11(47).
- Suslick, K.S. *et al.* 1991 'Sonochemical synthesis of amorphous iron', *Nature*, 353(6343), pp. 414–416. doi:10.1038/353414a0.
- Sono, T., Mingos, D. and Baghurst, D. 2004 'Novel energy source for reactions. In: The new chemistry.', *Cambridge:Syndicate of the University of Cambridge*. Edited by N. Hall.
- Qiu, L.-G. *et al.* 2008 'Facile synthesis of nanocrystals of a microporous metal-organic framework by an ultrasonic method and selective sensing of organoamines', *Chemical Communications*, (31), p. 3642. doi:10.1039/b804126a.
- Li, Z.-Q. *et al.* 2009 'Ultrasonic synthesis of the microporous metal-organic framework CU<sub>3</sub>(BTC)<sub>2</sub> at ambient temperature and pressure: An efficient and environmentally friendly method', *Materials Letters*, 63(1), pp. 78–80. doi:10.1016/j.matlet.2008.09.010.
- Lee, D.-E. *et al.* 2012 'Multifunctional nanoparticles for multimodal imaging and theragnosis', *Chem. Soc. Rev.*, 41(7), pp. 2656–2672. doi:10.1039/c2cs15261d.
- Cai, W. *et al.* 2018 'Metal-organic framework-based stimuli-responsive systems for Drug Delivery', *Advanced Science*, 6(1). doi:10.1002/advs.201801526.
- Lu, K. *et al.* 2018 'Nanoscale Metal-organic frameworks for therapeutic, imaging, and sensing applications', *Advanced Materials*, 30(37). doi:10.1002/adma.201707634.
- Winarta, J. *et al.* 2019 'A decade of UIO-66 research: A historic review of dynamic structure, synthesis mechanisms, and characterization techniques of an archetypal metal-organic framework', *Crystal Growth & Design*, 20(2), pp. 1347–1362. doi:10.1021/acs.cgd.9b00955.

Valenzano, L. *et al.* 2011 ‘Disclosing the complex structure of UiO-66 Metal Organic Framework: A SYNERGIC combination of experiment and theory’, *Chemistry of Materials*, 23(7), pp. 1700–1718. doi:10.1021/cm1022882.

Wu, H. *et al.* 2013 ‘Unusual and highly tunable missing-linker defects in zirconium metal–organic framework UIO-66 and their important effects on gas adsorption’, *Journal of the American Chemical Society*, 135(28), pp. 10525– 10532. doi:10.1021/ja404514r.

Furukawa, H. *et al.* 2013 ‘The chemistry and applications of metal-organic frameworks’, *Science*, 341(6149). doi:10.1126/science.1230444.

Platero-Prats, A.E. *et al.* 2016 ‘Structural transitions of the metal-oxide nodes within metal–organic frameworks: On the local structures of Nu-1000 and Uio- 66’, *Journal of the American Chemical Society*, 138(12), pp. 4178–4185. doi:10.1021/jacs.6b00069.

Choi, S. *et al.* 2016 ‘Isotropic and anisotropic growth of metal–Organic Framework (MOF) on MOF: Logical inference on MOF structure based on Growth Behavior and morphological feature’, *Journal of the American Chemical Society*, 138(43), pp. 14434–14440. doi:10.1021/jacs.6b08821.

Deshpande, M.S., Kumbhar, A.S. and Puranik, V.G. 2008 ‘Hydrogen bonding- directed metallosupramolecular structural motifs based on a peripheral urea fused bipyridine Tecton’, *Crystal Growth & Design*, 8(6), pp. 1952–1960. doi:10.1021/cg8000015.

Liang, W., Babarao, R. and D’Alessandro, D.M. 2013 ‘Microwave-assisted solvothermal synthesis and optical properties of tagged MIL-140A metal– organic frameworks’, *Inorganic Chemistry*, 52(22), pp. 12878–12880. doi:10.1021/ic4024234.

Klinowski, J. *et al.* 2011 ‘Microwave-assisted synthesis of metal–organic frameworks’, *Dalton Trans.*, 40(2), pp. 321–330. doi:10.1039/c0dt00708k.

Zou, D. and Liu, D. 2019 ‘Understanding the modifications and applications of highly stable porous frameworks via UIO-66’, *Materials Today Chemistry*, 12, pp. 139–165. doi:10.1016/j.mtchem.2018.12.004.

Kandiah, M. *et al.* 2010 ‘Post-synthetic modification of the metal–organic framework compound uio-66’, *Journal of Materials Chemistry*, 20(44), p. 9848. doi:10.1039/c0jm02416c.

Garibay, S.J. and Cohen, S.M. 2010 ‘ISORETICULAR synthesis and modification of frameworks with the UIO-66 topology’, *Chemical Communications*, 46(41), p. 7700. doi:10.1039/c0cc02990d.

Bueken, B. *et al.* 2017 ‘Tackling the defect conundrum in uio-66: A mixed- linker approach to engineering missing linker defects’, *Chemistry of Materials*, 29(24), pp. 10478–10486. doi:10.1021/acs.chemmater.7b04128.

Shearer, G.C. *et al.* 2016 ‘Defect engineering: Tuning the porosity and composition of the metal–organic framework UIO-66 via modulated synthesis’, *Chemistry of Materials*, 28(11), pp. 3749–3761. doi: 10.1021/acs.chemmater. 6b00602.

Thornton, A.W. *et al.* 2016 ‘Defects in metal–organic frameworks: A compromise between adsorption and stability?’, *Dalton Transactions*, 45(10), pp. 4352–4359. doi:10.1039/c5dt04330a.

Øien, S. *et al.* (2014a) ‘Detailed structure analysis of atomic positions and defects in zirconium metal–organic frameworks’, *Crystal Growth & Design*, 14(11), pp. 5370–5372. doi:10.1021/cg501386j.

Liu, L. *et al.* 2019 ‘Imaging defects and their evolution in a metal–organic framework at sub-unit-cell resolution’, *Nature Chemistry*, 11(7), pp. 622–628. doi:10.1038/s41557-019-0263-4.

Cliffe, M.J. *et al.* 2014 ‘Correlated defect nanoregions in a metal–organic framework’, *Nature Communications*, 5(1). doi:10.1038/ncomms5176.

Sun, C.-Y. *et al.* 2012 ‘Metal-organic frameworks as potential drug delivery systems’, *Expert Opinion on Drug Delivery*, 10(1), pp. 89–101. doi:10.1517/17425247.2013.741583.

Al Haydar, M. *et al.* 2018 ‘Multimetal organic frameworks as drug carriers: Aceclofenac as a drug candidate’, *Drug Design, Development and Therapy*, Volume 13, pp. 23–35. doi:10.2147/dddt.s182983.

Dastneshan, A. *et al.* 2023 ‘Cefazolin encapsulated UIO-66-NH<sub>2</sub> nanoparticles enhance the antibacterial activity and biofilm inhibition against drug-resistant *S. aureus*: In vitro and in vivo studies’, *Chemical Engineering Journal*, 455, p. 140544. doi:10.1016/j.cej.2022.140544.

Hartlieb, K.J. *et al.* 2017 ‘Encapsulation of ibuprofen in CD-MOF and related bioavailability studies’, *Molecular Pharmaceutics*, 14(5), pp. 1831– 1839. doi:10.1021/acs.molpharmaceut.7b00168.

Rakhshani, N. *et al.* 2021 ‘Fabrication of novel poly(n-vinylcaprolactam)- coated uio-66-NH<sub>2</sub> metal organic framework nanocarrier for the controlled release of doxorubicin against A549 lung cancer cells’, *Journal of Drug Delivery Science and Technology*, 66, p. 102881. doi:10.1016/j.jddst.2021.102881.

Khosravi, F. *et al.* 2023 ‘Ultrasensitive electrochemical mir-155 nanocomposite biosensor based on functionalized/conjugated graphene materials and gold nanostars’, *Sensors and Actuators B: Chemical*, 375, p. 132877. doi:10.1016/j.snb.2022.132877.

Moeinabadi-Bidgoli, K. *et al.* 2022 ‘Mesenchymal stem cell-derived antimicrobial peptides as potential anti-neoplastic agents: New insight into anticancer mechanisms of stem cells and exosomes’, *Frontiers in Cell and Developmental Biology*, 10. doi:10.3389/fcell.2022.900418.

Abánades Lázaro, I., Wells, C.J. and Forgan, R.S. 2020 ‘Multivariate modulation of the zr mof uio-66 for defect-controlled Combination Anticancer Drug Delivery’, *Angewandte Chemie*, 132(13), pp. 5249–5255. doi:10.1002/ange.201915848.

Liu, X. 2019 ‘Metal-organic framework UIO-66 membranes’, *Frontiers of Chemical Science and Engineering*, 14(2), pp. 216–232. doi:10.1007/s11705-019-1857-5.

Wu, M. *et al.* 2018 ‘Multistimuli responsive core–shell nanoplatfrom constructed from Fe<sub>3</sub>O<sub>4</sub>@mof equipped with pillar[6]arene nanovalves’, *Small*, 14(17). doi:10.1002/sml.201704440.

Zhou, T. *et al.* 2018 ‘Nanoscaled metal-organic frameworks for Biosensing, imaging, and cancer therapy’, *Advanced Healthcare Materials*, 7(10). doi:10.1002/adhm.201800022.

Wang, H. *et al.* 2019 ‘Formation of quasi-core-shell IN<sub>2</sub>S<sub>3</sub>/anatase tio<sub>2</sub>@metallic ti<sub>3</sub>c<sub>2</sub>x hybrids with favorable charge transfer channels for excellent visible-light-photocatalytic performance’, *Applied Catalysis B: Environmental*, 233, pp. 213–225. doi:10.1016/j.apcatb.2018.04.012.

Pourmadadi, M. *et al.* 2022 ‘Uio-66 metal-organic framework nanoparticles as gifted mofs to the biomedical application: A comprehensive review’, *Journal of Drug Delivery Science and Technology*, 76, p. 103758. doi:10.1016/j.jddst.2022.103758.

Huang, X. *et al.* 2006 ‘Ligand-directed strategy for zeolite-type metal–organic frameworks: Zinc(ii) imidazolates with unusual zeolitic topologies’, *Angewandte Chemie International Edition*, 45(10), pp. 1557–1559. doi:10.1002/anie.200503778.

Park, K.S. *et al.* 2006 ‘Exceptional Chemical and thermal stability of zeolitic imidazolate frameworks’, *Proceedings of the National Academy of Sciences*, 103(27), pp. 10186–10191. doi:10.1073/pnas.0602439103.

Phan, A. *et al.* 2009 ‘Synthesis, structure, and carbon dioxide capture properties of zeolitic imidazolate frameworks’, *Accounts of Chemical Research*, 43(1), pp. 58–67. doi:10.1021/ar900116g.

Venna, S.R., Jasinski, J.B. and Carreon, M.A. 2010 ‘Structural evolution of zeolitic imidazolate framework-8’, *Journal of the American Chemical Society*, 132(51), pp. 18030–18033. doi:10.1021/ja109268m.

- Banerjee, R. *et al.* 2009 ‘Control of pore size and functionality in isorecticular zeolitic imidazolate frameworks and their carbon dioxide selective capture properties’, *Journal of the American Chemical Society*, 131(11), pp. 3875–3877. doi:10.1021/ja809459e.
- Troyano, J. *et al.* 2019 ‘Colloidal metal–organic framework particles: The pioneering case of zif-8’, *Chemical Society Reviews*, 48(23), pp. 5534–5546. doi:10.1039/c9cs00472f.
- Schelling, M. *et al.* 2020 ‘Synthesis of a zinc–imidazole metal–organic framework (zif-8) using zno rods grown on cotton fabrics as precursors: Arsenate Absorption Studies’, *Cellulose*, 27(11), pp. 6399–6410. doi:10.1007/s10570-020-03216-4.
- Pouramini, Z. *et al.* 2023 ‘Effect of metal atom in zeolitic imidazolate frameworks (Zif-8 & 67) for removal of dyes and antibiotics from wastewater: A Review’, *Catalysts*, 13(1), p. 155. doi:10.3390/catal13010155.
- Bradford, M. M. 1976. A rapid and sensitive method for the quantitation of microgram quantities of protein utilizing the principle of protein-dye binding. *Analytical Biochemistry*, 72(1–2), 248–254. doi:10.1016/0003-2697(76)90527-3
- Choi, H. S., Liu, W., Liu, F., Nasr, K., Misra, P., Bawendi, M. G., & Frangioni, J.V. 2010. Design considerations for tumour-targeted nanoparticles. *Nature Nanotechnology*, 5(1), 42–47. <https://doi.org/10.1038/nnano.2009.314>
- Chowdhuri, A. R., Laha, D., Pal, S., Karmakar, P., & Sahu, S. K. 2016. One-pot synthesis of folic acid encapsulated upconversion nanoscale metal organic frameworks for targeting, imaging and pH responsive drug release. *Dalton Transactions*, 45(45), 18120–18132. doi:10.1039/C6DT03237K
- Gao, S., Zheng, P., Li, Z., Feng, X., Yan, W., Chen, S., Guo, W., Liu, D., Yang, X., Wang, S., Liang, X.-J., & Zhang, J. 2018. Biomimetic O<sub>2</sub>-Evolving metal-organic framework nanoplatform for highly efficient photodynamic therapy against hypoxic tumor. *Biomaterials*, 178, 83–94. doi:10.1016/j.biomaterials.2018.06.007
- Hoop, M., Walde, C. F., Riccò, R., Mushtaq, F., Terzopoulou, A., Chen, X.-Z., deMello, A. J., Doonan, C. J., Falcaro, P., Nelson, B. J., Puigmartí-Luis, J., & Pané, S. 2018. Biocompatibility characteristics of the metal organic framework ZIF-8 for therapeutical applications. *Applied Materials Today*, 11, 13–21. doi:10.1016/j.apmt.2017.12.014
- Karakeçili, A., Topuz, B., Korpayev, S., & Erdek, M. 2019. Metal-organic frameworks for on-demand pH controlled delivery of vancomycin from chitosan scaffolds. *Materials Science and Engineering: C*, 105, 110098. doi:10.1016/j.msec.2019.110098

- Kaur, H., Mohanta, G. C., Gupta, V., Kukkar, D., & Tyagi, S. 2017. Synthesis and characterization of ZIF-8 nanoparticles for controlled release of 6- mercaptopurine drug. *Journal of Drug Delivery Science and Technology*, 41, 106– 112. doi:10.1016/j.jddst.2017.07.004
- Motegi, H., Yano, K., Setoyama, N., Matsuoka, Y., Ohmura, T., & Usuki, A. 2017. A facile synthesis of UiO-66 systems and their hydrothermal stability. *Journal of Porous Materials*, 24(5), 1327–1333. doi:10.1007/s10934-017- 0374-5
- Pan, Y., Liu, Y., Zeng, G., Zhao, L., & Lai, Z. 2011. Rapid synthesis of zeolitic imidazolate framework-8 (ZIF-8) nanocrystals in an aqueous system. *Chemical Communications*, 47(7), 2071. doi:10.1039/c0cc05002d
- Riduan, S., & Zhang, Y. 2021. Recent advances of zinc-based antimicrobial materials. *Chem. Asian J.* 16, 2588–2595.
- Zheng, X., Zhang, Y., Zou, L., Wang, Y., Zhou, X., Yao, L., Wang, Z., Li, C., & Qiu, Y. 2020. Robust ZIF-8/alginate fibers for the durable and highly effective antibacterial textiles. *Colloid Surf. B-Biointerfaces*. 193.
- Yao, S., Chi, J., Wang, Y., Zhao, Y., Luo, Y., & Wang, Y. 2021. Zn-MOF encapsulated antibacterial and degradable microneedles array for promoting wound healing. *Adv. Healthc. Mater.* 10, Article e2100056.
- Mendes, C., Dilarri, G., Forsan, C., Sapata, V., Lopes, P., de Moraes, P., Montagnolli, R., Ferreira, H., & Bidoia, E. 2022. Antibacterial action and target mechanisms of zinc oxide nanoparticles against bacterial pathogens. *Sci. Rep.* 12.
- Burch, N., Jasuja, H., & Walton, K. 2014. Water stability and adsorption in metalorganic frameworks. *Chem. Rev.* 114 (20), 10575–10612.
- Zeng, X., Yan, S., & Liu, B.-F. 2022. *Microporous Mesoporous Mater.* 335, Article e111826.
- Yu, D., et al. 2020. *Biomaterials* 255, Article e120160.
- Wang, J., et al. 2023. *Adv. Sci.* 10, Article 2206854.
- Bai, Q., et al. 2024. *Adv. Healthcare Mater.* 13.
- Elrasheedy, A., Nady, N., Bassyouni, M., & El-Shazly, A. 2019. Metal- organic framework based polymer mixed matrix membranes: Review on applications in water purification. *Membranes*, 9(7), 88. <https://doi.org/10.3390/membranes9070088>